

Deterministic criticality & cluster dynamics hidden in the Game of Life

Hakan Akgün,¹ Xianquan Yan (颜显权),^{2,3} Tamer Taşkıran,⁴ Muhamet Ibrahim,⁵ Arash Mobaraki,⁴ Ching Hua Lee,^{2,*} and Seymur Jahangirov^{4,†}

¹*Department of Physics, Bilkent University, Ankara, Turkey*

²*Department of Physics, National University of Singapore, Singapore 117551*

³*Department of Computer Science, National University of Singapore, Singapore 117417*

⁴*UNAM, Institute of Materials Science and Nanotechnology, Bilkent University, Ankara 06800, Turkey*

⁵*Laboratory of Artificial and Natural Evolution (LANE), Department of Genetics and Evolution, University of Geneva, 1211 Geneva, Switzerland*

(Dated: November 12, 2024)

Conway’s Game of Life (GOL) is a cellular automaton showing how complex dynamical behavior emerges from simple local interactions. Although it has often been shown that the dynamics of GOL lies close to some sort of critical behavior, this system has never been studied in the context of a deterministic phase transition. Here, we study the critical dynamics of equal-state clusters that emerge in the *logistic* GOL: an extension of Conway’s GOL with a parameter that alters the dynamics by expanding the binary state space into a Cantor set, while maintaining the deterministic nature of the system. Upon tuning the parameter, we find that the logistic GOL comprises at least three types of asymptotic behavior, *i.e.* phases, that are separated by two critical points. One critical point defines the boundary between a sparse-static and a sparse-dynamic asymptotic phase, whereas the other point marks a deterministic percolation transition between the sparse-dynamic and a third, dense-dynamic asymptotic phase. Moreover, we identify distinct power-law distributions of cluster sizes near the critical points, and discuss the underlying mechanisms that give rise to such critical behavior. Overall, our work highlights the idea that scale invariance can emerge even in systems where clusters are generated by a purely deterministic process.

I. INTRODUCTION

Criticality has always been associated with universal scaling behavior and universality classes in non-equilibrium systems [1–7]. In particular, deterministic criticality has been a focal point for structures that emerge from fixed rules, particularly in the context of percolation, a theme which has itself united various branches of mathematics [8–12] and physics [13–31]. Deterministic criticality plays a crucial role in understanding how systems governed by fixed rules can exhibit complex behaviors, including phase transitions and scaling laws, without relying on randomness. It has been examined through deterministic processes governing invasion percolation [32], electrical [33] and elastic [34] responses in deterministic fractal networks, as well as deterministic ansatz for fractal-like critical snapshots [35]. Moreover, it has also been demonstrated in deterministic walks, sand-pile models [36, 37], bootstrap percolation on trees with hierarchical dynamics [38, 39].

In this work, we report the surprising emergence of deterministic criticality in a closed Game of Life (GOL) system, a cellular automaton governed by exceedingly simple deterministic evolution rules. First introduced in 1970 [40, 41], this discrete dynamical system initially gained attention as (i) an exquisite illustration of the idea that complex behavior can emerge from simple interactions, and as (ii) a universal Turing ma-

chine [42, 43]. Moreover, Conway’s GOL has been often considered an elegant starting point for studying emergent phenomena such as artificial life [44–47], neural networks [48], ecology [49, 50] self-organization [51–54], quantum systems [55–58], criticality [59–61] and phase transitions [62–68].

Conway’s GOL has been widely investigated in the context of a phase transition because it is an inherently complex system. Indeed, the long transient dynamics and localized structures – that emerge from parallel local interactions (*i.e.* automaton rules) among binary states in a square lattice of sites – support the notion that this system resides between ‘order and chaos’ [69]. However, statistical investigations [64, 70, 71] have revealed that GOL is *subcritical* in terms of its late time behavior, with an asymptotic density significantly lower than the mean-field prediction [68]. In this respect, it has been tempting to introduce extensions of GOL with control parameters that, by incrementally modifying the automaton rules away from the original system, can identify how far the GOL dynamics is from a critical phase transition. Examples of such extensions include asynchronous [62] or mass-conserving [63] update schemes, probabilistic rules of time evolution [64–66], varying ranges of interactions [67], etc., and find that the rules of GOL are close to both continuous and discontinuous critical phase transitions. However, while most of these extensions are variations that employ probabilistic/random components, this deterministic automaton has never been investigated in the context of a deterministic phase transition [72, 73].

In this paper, we analyze the phase transitions that occur in the *logistic* GOL [53]: an extension inspired by the

* phylch@nus.edu.sg

† seyumur@unam.bilkent.edu.tr

logistic map [74], where a control parameter changes the rate of update of sites by expanding the initially binary state space into a Cantor set. As the parameter ‘drifts’ the system away from Conway’s GOL, its asymptotic dynamics transitions from a sparse-inactive (I) phase (like Conway’s GOL) to a sparse-active (II), and then a dense-active (III) phase. We identify the points that separate these three distinct dynamical regimes numerically and study their critical properties by in-depth analyses of cluster dynamics. We find that the critical point separating phases I and II defines the bound of a peculiar form of self-organized criticality in the sparse-active phase, where quiescent clusters surrounded by activity follow a power-law distribution. Moreover, detailed cluster analyses at the critical point separating phases II and III, indicate a deterministic, continuous percolation transition. Interestingly, the identified percolation exhibits a Fisher exponent below two, differing from random percolation models and aligning with no enclave percolation [75]. Beyond showcasing critical behavior in deterministic dynamical systems, the logistic GOL introduces a broad range of deterministic tunability. This tunability allows for precise control of the cluster shapes and the ‘fatness’ of cluster size distributions, studied here for the first time in a variation of GOL.

The paper is organized as follows. In Sec. II we discuss how we extend Conway’s GOL to the logistic GOL. In Sec. III, we report results from simulations of the logistic GOL and identify the different asymptotic dynamical regimes separated by critical points. In Sec. IV, we perform extensive cluster analyses and to study the percolation transition between phases II and III, whereas in Sec. V we investigate both critical points in terms of their power-law cluster size distributions. Lastly, in Sec. VI we provide a summary and discussion on the deterministic critical behavior identified in the logistic GOL.

II. THE LOGISTIC GAME OF LIFE

Conway’s GOL is defined on a square grid of sites, where each site goes through the parallel updating scheme:

$$s_j^{t+1} = s_j^t + \Delta s_j, \quad (1)$$

where $s_j^t \in \{0, 1\}$ corresponds to the state of j^{th} site at time point t . Δs_j denotes the state update, and is a function of s_j^t itself and the sum of states in its Moore neighborhood, m_j^t (Fig. 1a left panel). If we formulate the rules (*i.e.*, the time evolution) of Conway’s GOL [40] in the finite-difference form of Eq. (1), a site will experience three possible updates: decay ($\Delta s_j = -s_j$ when $m_j < 2$ or $m_j > 3$), stability ($\Delta s_j = 0$ when $m_j = 2$), or growth ($\Delta s_j = 1 - s_j$ when $m_j = 3$) (Fig. 1a right).

Motivated by the well-known logistic map [74], logistic Game of Life [53] stands as a prominent candidate to study and investigate critical behaviors and clus-

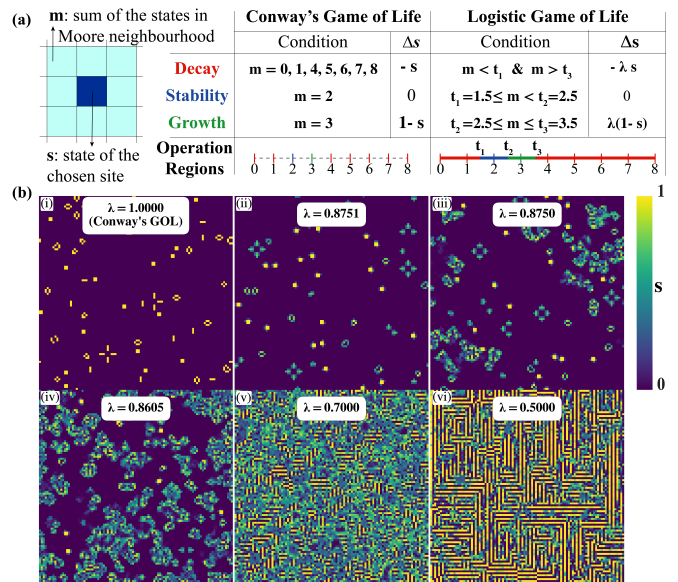


FIG. 1. **The logistic Game of Life.** (a) Short summary of the rules of Conway’s GOL (left) and the logistic GOL (right). In the latter, a parameter λ tunes the rate of update of sites. (b) Snapshots of the asymptotic state in both Conway’s Game of Life ($\lambda = 1$) and the Logistic Game of Life across various λ values. Each configuration was initialized with random arrays on a 1024×1024 grid and evolved for 10000 time steps.

ter dynamics in critical settings, while preserving deterministic update rules. Logistic GOL extends GOL by introducing a parameter λ that re-scales the updates, *i.e.*, the growth/decay rate of each site. More formally, $\Delta s_j^t \rightarrow \lambda \Delta s_j^t$, where $0 < \lambda \leq 1$ and $\lambda = 1$ is the limit corresponding to Conway’s GOL (Fig. 1a right).

An important consequence of λ in the logistic GOL is that the previously binary state space of the automaton expands into a Cantor set. To see this, we define a simple representation that associates the three possible updates to discrete operators, respectively to decay (**D**), stability (**S**) and growth (**G**), such that:

$$\mathbf{D}s := (1 - \lambda)s, \quad \mathbf{S}s := s, \quad \mathbf{G}s := (1 - \lambda)s + \lambda. \quad (2)$$

In other words, the discrete operators show how the state s of a site may transform, based on the λ -dependent update (Fig. 1a right). If we apply these operators to an initial set of $\{0, 1\}$ once, they give rise to a larger set $\{0, 1 - \lambda, \lambda, 1\}$. Again, applying operators to the new set gives rise to $\{0, (1 - \lambda)^2, (1 - \lambda) - (1 - \lambda)^2, 1 - \lambda, \lambda, \lambda + (1 - \lambda)^2, \lambda, 1 - (1 - \lambda)^2, 1\}$. Repeating this recursively would lead to a Cantor set in the range $[0, 1]$. The Cantor set (Fig. 1b) is λ -dependent and each element in the set can be assigned to an order that denotes the times a **D**/**G** operator has been applied. For example, $\mathbf{GG}0 = 1 - (1 - \lambda)^2$ is a second-order Cantor value (Fig. 1b).

A second consequence of λ is that, due to the expanded state space, the space of neighborhood sums m (which determine how sites are updated) is also expanded. In

the logistic GOL, possible m values span the range $[0, 8]$ and comprise an eight-fold convolution of the Cantor set. To account for this, we assign two unit-length intervals centered at $m = 2$ and $m = 3$ to assign the neighborhood sum regions of stability and growth, respectively (Fig. 1b). We denote the limits of these intervals by $t_1 = 1.5, t_2 = 2.5$, and $t_3 = 3.5$, such that sites get updated in the following fashion:

$$s_j^{t+1} = \begin{cases} \mathbf{S}s_j^t = s_j^t & \text{if } t_1 \leq m_j^t < t_2 \\ \mathbf{G}s_j^t = (1 - \lambda)s_j^t + \lambda & \text{if } t_2 \leq m_j^t \leq t_3 \\ \mathbf{D}s_j^t = (1 - \lambda)s_j^t & \text{otherwise} \end{cases} \quad (3)$$

The rules of Conway's and logistic GOL are summarized in Fig. 1a, and snapshots of asymptotic behavior of the logistic GOL are displayed in Fig. 1b. It has been previously identified [53] that the dynamic and asymptotic behavior of logistic GOL for $0.875 < \lambda < 1$ is similar to Conway's GOL, where the system settles to a sparse inactive asymptotic state. Whereas, for $\lambda \leq 0.875$, the system possesses active asymptotic states, which increasingly cover the system as λ decreases (Fig. 1c).

To investigate the asymptotic dynamics in detail, we perform simulations of the logistic GOL where the state space is truncated up to the 10th order of the Cantor set. In other words, during simulations, any state with a higher-order Cantor value is "lumped" into the nearest Cantor value of order ≤ 10 (see Appendix IX for implementation). As reported in following sections, this modification makes it possible to perform cluster analyses of the system while maintaining the features of logistic GOL with an un-truncated Cantor set.

III. SIGNS FOR CRITICAL BEHAVIOR

In this section, we study the asymptotic behavior of the logistic GOL, which exhibits remarkable changes as the control parameter λ 'drifts' the system away from Conway's GOL (see the different panels in Fig. 1b). To investigate whether such changes in the asymptotic behavior are related to critical phenomena, below we define quantities that characterize the dynamics of the system.

First, we define an *activity* order parameter, A , of the following form:

$$A^t := 1 - \frac{1}{N^2} \sum_j \delta_{s_j^t, s_j^{t-\bar{t}}}, \quad (4)$$

where N denotes the length of the square lattice, $\delta_{,\prime}$ denotes the Kronecker delta, and the sum is over all sites. A is thus defined to denote the fraction of cells that change states after a time lag \bar{t} , serving as a measure of lattice's autocorrelation. In the following, we set $\bar{t} = 60$ to exclude asymptotic-state oscillators with periods that are divisors of 60. We then average the activity over time and ensemble to obtain $\langle A \rangle$. Thus, $\langle A \rangle = 1$ indicates that there is no autocorrelation between the states and

their time-lagged counterparts, whereas $\langle A \rangle = 0$ reflects perfect autocorrelation, *i.e.* the grid's time-lagged version is identical to the current state.

Second, we use the definition of Eq. (4) to characterize the spatial variation of activity through the *susceptibility*, defined as the fluctuation of the order parameter:

$$\langle \chi \rangle := \langle A^2 \rangle - \langle A \rangle^2. \quad (5)$$

Analogous to magnetic systems, the susceptibility measures how uniformly the activity is distributed across the lattice. A system comprising of only a few localized active sites is characterized by a high susceptibility, whereas a uniform distribution of active sites leads to a vanishing susceptibility.

Third, we define *clusters* to identify groups of equal-state sites that are connected through their direct nearest neighbors, *i.e.* up, down, left or right first neighbors. More precisely, a cluster C^t denotes a set of sites in the lattice such that, for any two sites $j, j' \in C^t$, there exists at least one sequence $\{j, k, l, \dots, j'\}$ where

$$s_j^t = s_k^t = s_l^t = \dots = s_{j'}^t, \quad (6)$$

and each site is the direct nearest neighbor of at least one other site in C^t . Moreover, C^t is defined such that it is the maximal set of connected sites satisfying the clustering condition, and no subset $\bar{C}^t \subsetneq C^t$ is considered a separate cluster. We moreover define the size of a cluster S^t , denoting the number of sites in the cluster, *i.e.*, the cardinality of C^t :

$$S^t = n(C^t). \quad (7)$$

Finally, the cluster size ranking at a given time point is defined by the ordering $S_1^t \geq S_2^t \geq S_3^t \geq \dots \geq S_i^t \geq \dots$, where the index i here indicates the size rank of the cluster. The cluster sizes are then averaged over time and ensemble to obtain $\langle S_i \rangle$.

In Fig. 2, we report the numerically computed asymptotic quantities of $\langle A \rangle, \langle \chi \rangle$ and $\langle S_1 \rangle$ for the logistic GOL, where λ is a control parameter. We focus on the parameter region $0.8 < \lambda < 0.9$, where we notice signs of critical behavior at $\lambda_P = 0.86055$ and $\lambda_A = 0.8750$ and identify three distinct asymptotic phases of the system. In the following, we describe the changes of the system as λ is decreased.

First, we discuss how the average asymptotic activity $\langle A \rangle$ changes in the logistic GOL as λ is tuned down (blue data points in Fig. 2a). We observe that $\langle A \rangle \simeq 0$ for $\lambda < \lambda_A = 0.8750$, indicating that, in this parameter range, the logistic GOL comprises inactive asymptotic states. Indeed, similarly to Conway's GOL, the system settles to an inactive phase, *i.e.* a phase that is mostly populated by the *vacuum* background of quiescent states, and sparsely populated by stable blocks and periodic oscillators (see also panels i and ii in Fig. 1b). At $\lambda = \lambda_A$ we observe a sudden increase in activity, which indicates that the asymptotic dynamics becomes fundamentally different. In the $\lambda \leq \lambda_A$ range, the system does not

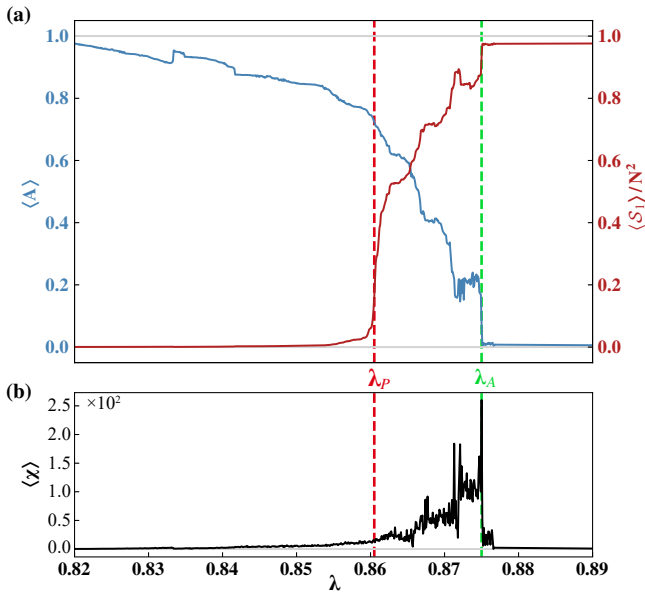


FIG. 2. **Distinct dynamical regimes in the logistic GOL are separated by two critical points.** (a) Asymptotic averaged activity $\langle A \rangle$ (light blue) and the size of the largest cluster $\langle S_1 \rangle / N^2$ (dark red) computed against λ . The data indicates at least two points of phase transitions: (i) $\lambda_P = 0.86055$ (red dashed line), where the size of largest cluster changes most drastically; (ii) $\lambda_A = 0.8750$ (green dashed line), the boundary between a zero and finite asymptotic activity. (b) The susceptibility of activity $\langle \chi \rangle$, plotted against λ , hits its maximum at λ_A .

settle into an inactive phase (panel iii in Fig. 1b), but it persists indefinitely in the thermodynamic limit. Moreover, we find that the susceptibility $\langle \chi \rangle$ reaches its maximum at $\lambda = \lambda_A$ (Fig. 2b). The sudden jump in $\langle A \rangle$ and maximal $\langle \chi \rangle$ (green dashed line in Fig. 2) suggest that λ_A is the critical point which marks the inactive-active transition in the asymptotic behavior of the system.

Besides defining the transition point between inactive and active phases in the logistic GOL, the asymptotic susceptibility $\langle \chi \rangle$ provides additional insights on the nature of this transition. The fact that $\langle \chi \rangle$ increases sharply from zero to a maximum as λ hits λ_A (Fig. 2b), indicates that the asymptotic activity at the transition point is initially localized in a very low number sites, and that the lattice is otherwise similar to the inactive phase in $\lambda_A < \lambda \leq 1$ (see also panel iii in Fig. 1b). Moreover, the drop of $\langle \chi \rangle$ as λ is decreased below λ_A , indicates that the activity becomes increasingly more spread in the lattice, until the entire space becomes homogeneously active and $\langle \chi \rangle$ hence vanishes (see panels iv and v in Fig. 1b and Fig. 2b).

Next, we identify a third asymptotic phase which emerges as λ is tuned down even further. In particular, we investigate the how the size of the largest cluster $\langle S_1 \rangle / N^2$ – *i.e.* corresponding to the vacuum cluster of quiescent states in the lattice – changes against λ . As shown in Fig. 2a (red data points), the vacuum cluster

λ	Transition	Neighborhood
0.86055	G \leftrightarrow D	$t_3 \approx -3\lambda^5 + 16\lambda^4 - 34\lambda^3 + 33\lambda^2 - 17\lambda + 8$
0.86055	S \leftrightarrow D	$t_1 \approx -3\lambda^5 + 16\lambda^4 - 34\lambda^3 + 33\lambda^2 - 17\lambda + 6$
0.8750	G \leftrightarrow D	$t_3 = 4\lambda$
0.8750	S \leftrightarrow D	$t_1 = 4[1 - \lambda] + 1$

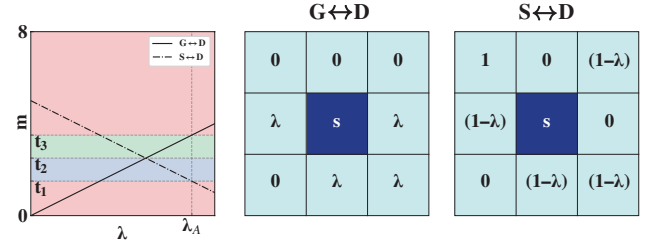


FIG. 3. **Operational transitions in neighborhoods at critical points** The table above presents the neighborhood sums corresponding to the critical points. The panel below shows neighborhoods undergoing transition, with individual site values highlighted around $\lambda_A = 0.875$, while the lower left panel illustrates the numerical evolution of these neighborhoods as λ varies between $0 < \lambda < 1$. For a similarly detailed view of the neighborhood at λ_P , see Appendix X

covers most of the grid when $\lambda > \lambda_A$. As λ is tuned down below λ_A , the size of the largest vacuum cluster drops in a fashion that corresponds exactly to the ‘inverse’ pattern of $\langle A \rangle$. However, as λ is tuned further, the behavior of $\langle S_1 \rangle / N^2$ becomes remarkably different as compared to $\langle A \rangle$. The largest cluster of quiescent states experiences a sharp decrease, where the strongest drop occurs at $\lambda_P = 0.86055$, defining another critical point. This sharp decrease in the size of the largest cluster (red dashed line in Fig. 2) is important because it indicates a transition from an asymptotic dynamical phase with the vacuum cluster spanning the lattice, to a dynamical phase where there is no spanning cluster, and is reminiscent of a percolation transition. We study this transition in detail below in Sec. IV. In addition, we note that the decrease in $\langle \chi \rangle$ (Fig. 2b) as λ goes below λ_P implies that the activity starts to spread uniformly within the lattice, and is another indicator of two distinct types of asymptotic behavior.

The increase in activity and the decrease of the vacuum cluster’s size indicates that the average density of the system increases as λ is tuned down (see also Fig. 1b). This occurs because, as λ decreases, there are several neighborhood configurations which change their operation regions (Fig. 3). For example, a neighborhood m_j consisting of $4 \times \lambda$ sites and 4×0 sites would ‘act’ to decay the central site if $\lambda > \lambda_A$ because $m_j = 4\lambda > t_3 = 3.5$. However, for $\lambda \leq \lambda_A$, then $m_j \leq t_3$, indicating that the central site will experience growth. In a similar fashion, another neighborhood with $m_k = 1 + 4(1 - \lambda)$ changes the operation region between decay and stability at λ_A .

In this case, the central site will decay when $\lambda > \lambda_A$, as $m_k < t_1 = 1.5$; and it will remain stable when $\lambda \leq \lambda_A$, as $m_k \geq t_1$. Note that there is a large set of neighborhood sums which changes operation regions as λ is being tuned, and it is these changes which alter the dynamics of the logistic GOL as λ is tuned [53]. The main neighborhood sums that change operation regions at $\lambda = \lambda_P$ are reported in Fig. 3. The discrete transition at λ_A is characterized by a 1st-order Cantor set polynomial Moore neighborhood, whereas the continuous percolation transition of the vacuum cluster stems from gradual neighborhood changes, emerging from higher-order Cantor set polynomial elements. As the percolation point is refined to greater decimal accuracy, increasingly higher-order Cantor set elements are required to characterize the associated polynomial neighborhood. For the explicit fifth-order neighborhood of λ_P and the methodology used to determine it, refer to Appendix X. These gradual operational transitions in neighborhood configurations with λ govern the evolution of cluster shape, size, and scaling. The following section explores how these transitions shape the behaviors of cluster shape, size, and scaling as λ varies.

IV. A DETERMINISTIC PERCOLATION TRANSITION IN THE LOGISTIC GOL

Motivated by the asymptotic behavior of the size of the largest cluster in the logistic GOL, we study here the cluster dynamics of the system as λ approaches λ_P from below. By investigating the sizes and geometrical properties of clusters, we find that λ_P is the critical point of a percolation transition that separates two distinct phases of asymptotic behavior: an active asymptotic phase with no spanning cluster ($\lambda \leq \lambda_P$) and an active asymptotic phase with a giant vacuum cluster that spans the lattice ($\lambda_P < \lambda < \lambda_A$).

We examine the size and geometrical properties of the largest clusters in the parameter range $\lambda \in [0.850, 0.875]$, where for brevity, we focus on the five largest clusters (Fig. 4). First, we note that the highest-ranked clusters, *i.e.* clusters with $\{\langle S_1 \rangle, \dots, \langle S_5 \rangle\}$, are all composed of zero states (see top and bottom panels in Fig. 4a). When $\lambda \simeq 0.85$, all the clusters share similar small sizes relatively to the lattice size (Fig. 4b). As λ increases and approaches λ_P , the size of every cluster increases, and the size of the second largest cluster hits maximum at $\lambda = \lambda_P$ (purple curve in Fig. 4b). When $\lambda > \lambda_P$, the size of the largest cluster increases (red regions in Fig. 4a and inset in Fig. 4b), while sizes of lower ranked clusters drop significantly.

Next, we analyze the evolution of the capacity dimension across λ to quantify changes in the shapes of the largest clusters. This analysis ‘probes’ whether clusters become scale-invariant near λ_P . Employing the box-counting method, we calculate the capacity dimensions

of the clusters:

$$d_c = - \lim_{\epsilon \rightarrow 0^+} \frac{\log \mathcal{N}(\epsilon)}{\log \epsilon} \quad (8)$$

where $\mathcal{N}(\epsilon)$ denotes the minimum number of boxes of size ϵ needed to cover the cluster (see Appendix XI A for methods). A capacity dimension $d_c \sim 1$ indicates that cluster shapes are more chain-like and sparse, while $d_c \sim 2$ indicates that clusters are more area-like and dense. The capacity dimensions of the largest five clusters are plotted against λ in Fig. 4c. The obtained values draw close to each other as λ approaches λ_P from below, and then separate when $\lambda > \lambda_P$. In this range, the largest cluster’s capacity dimension increases, while the other clusters’ capacity dimensions decrease.

Moreover, we examine how different samplings of the same clusters change at each λ by calculating the standard deviation of the capacity dimension σ_c . This allows us to quantify the stability of the shapes within a given cluster distribution. As shown in Fig. 4d the σ_c of every cluster decreases and reaches its minimum as λ approaches λ_P from below. When $\lambda > \lambda_P$, the largest cluster’s standard deviation remains stable over different samplings while σ_c of the other clusters increase. We note that such fluctuations are also reflected in the susceptibility profile seen in Fig. 2b.

The analysis of cluster shapes in the logistic GOL indicates that the highest-ranked cluster percolates at λ_P . Indeed, as λ approaches λ_P from below, the capacity dimensions of all clusters increase: they attain the same value and a minimal standard deviation ($d_c \approx 1.610$, $\sigma_c \approx 0.01$). In other words, when $\lambda = \lambda_P$, the shape of a cluster at a given time point is similar to the shape of any other cluster at any time point. Therefore, the clusters tend towards the same shape with respect to each other and only differ in size, providing evidence for scale invariance at λ_P . Then, when $\lambda > \lambda_P$, the shapes clusters change drastically with respect to each other (Fig. 4c) and with respect to their different samples (Fig. 4d). Here, the increase of the largest cluster’s size and capacity dimension (dark red in Fig. 4a,c and Appendix Fig. 11) signals the percolation transition, whereas the sizes and capacity dimensions of the smaller clusters decrease as they become smaller and more chain-like.

To further support the idea that the transition at λ_P is percolation-like, we investigate how the largest cluster’s size $\langle S_1 \rangle$ scales with the lattice size N close to λ_P (Fig. 4e), where we find that the scaling is the same as in classical percolation models [76, 77]. While delegating the methods and details in Appendix XI B, here we report the observed scaling relationships:

$$\langle S_1(N) \rangle \sim \begin{cases} \log N, & \text{for } \lambda < \lambda_P, \\ N^{d_f}, & \text{for } \lambda = \lambda_P, \\ N^D, & \text{for } \lambda > \lambda_P, \end{cases} \quad (9)$$

where $D = 2$ denotes the dimension of the system, and $d_f < D$ defines what is referred as the fractal dimension. In the ‘subcritical’ regime ($\lambda < \lambda_P$), the largest

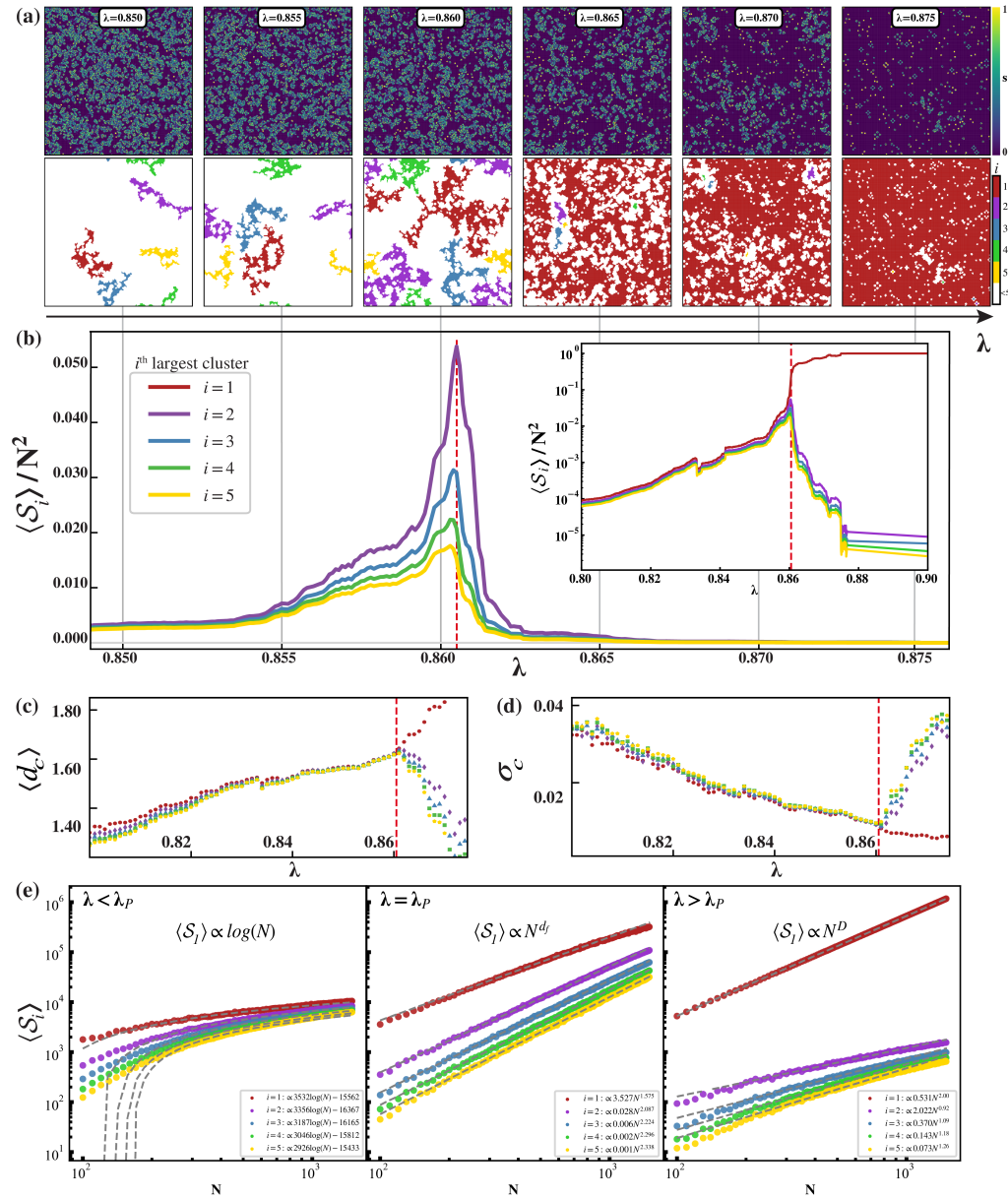


FIG. 4. **Deterministic cluster dynamics indicates a percolation transition hidden in the logistic GOL.** (a) Top panels display snapshots of the asymptotic states of the logistic GOL at distinct λ values in the range $[0.850, 0.875]$. Bottom panels show the corresponding five largest clusters masked in different colors (ranking in panel b). (b) Sizes of the largest clusters $\langle S_2 \rangle \sim \langle S_5 \rangle$ plotted against λ . The curves differ only by scaling when $\lambda < \lambda_P$. The inset displays the logarithmic evolution of cluster sizes, with the largest zero-state cluster (dark red) percolating as λ increases. The evolution of (c) capacity dimensions d_c of the largest clusters and their (d) corresponding standard deviations σ_c computed as functions of λ . (e) Scaling behavior of the largest cluster with lattice size (N) around λ_P . In the ‘subcritical’ regime ($\lambda < \lambda_P$, left), cluster sizes $\langle S_i(N) \rangle$ follow a logarithmic trend. Around the critical point ($\lambda = \lambda_P$, middle), the clusters scale as power laws, where the exponent of the largest cluster defines the fractal dimension d_f . In the ‘supercritical’ regime ($\lambda > \lambda_P$, right), the largest cluster $\langle S_1 \rangle$ scales with the system’s dimension, spanning the lattice. The associated fits are shown with gray dashed lines.

cluster grows logarithmically with system size (left panel in Fig. 4e), meaning that there can be no giant cluster spanning the lattice. At the critical point ($\lambda = \lambda_P$), the largest cluster follows a fractal scaling, reflecting the self-similar nature of the percolating cluster (Fig. 4e middle panel). The fitted fractal dimension is $d_f \approx 1.575$ with a

standard deviation of $\sigma_f \approx 0.1$, attributed to deviations from the exact critical point λ_P beyond five decimal precision, which also cause deviations in the large N regime. In the ‘supercritical’ regime ($\lambda > \lambda_P$), the largest cluster grows with the system dimension ($D = 2$), indicating the formation of a percolating cluster that spans the lattice

(Fig. 4e right panel).

Besides the scaling relations governing $S_1(N)$, the scalings of lower-ranked clusters $\langle S_i(N) \rangle$ indicate that, as $N \rightarrow \infty$, $\langle S_i(N) \rangle$ diverge to infinity only at the critical point $\lambda = \lambda_P$ (Fig. 4e). Furthermore, the divergence of the second largest peak is explicitly shown in Appendix XIC. Taken together, all the analyses of largest clusters (Fig. 4) signal for the emergence of percolating cluster and a phase transition [78].

V. CLUSTER SIZE DISTRIBUTIONS NEAR THE CRITICAL POINTS

In this section, we investigate whether the cluster size distributions near the critical points λ_P and λ_A follow power laws. To do this, we perform numerical simulations of the logistic GOL to compute the distribution of cluster sizes, $p(\mathcal{S})$, in the vicinity of each critical point (Fig. 13, Appendix). At $\lambda_P = 0.86055$, $p(\mathcal{S})$ seems to follow a power law, while other λ values around it appear as stretched exponentials (Fig. 13a). On the other hand, there are multiple λ values close to $\lambda_A = 0.8750$ where the distributions are reminiscent of power laws, but only if the largest vacuum clusters are disregarded (Fig. 13b). While delegating technical aspects on computations of $p(\mathcal{S})$ to Appendix XID, below we leverage quantitative methods to test whether such distributions are indeed best described by power laws.

The scaling of empirical power-law data is rarely valid across the entire domain of cluster sizes. More often, the power law applies only for values greater than some lower bound \mathcal{S}_{\min} , *i.e.*, only the ‘tail’ follows a power law. In such cases, the cluster size distribution is expected to follow:

$$p(\mathcal{S}) = \frac{\mathcal{S}^{-\tau}}{\zeta(\tau, \mathcal{S}_{\min})} \quad \text{for } \mathcal{S} \geq \mathcal{S}_{\min} \quad (10)$$

where τ is the power-law exponent (the Fisher exponent [79]), \mathcal{S}_{\min} is the lower cutoff, and $\zeta(\tau, \mathcal{S}_{\min})$ denotes the generalized zeta function

$$\zeta(\tau, \mathcal{S}_{\min}) = \sum_{\mathcal{S}=\mathcal{S}_{\min}}^{\infty} \mathcal{S}^{-\tau} = \sum_{\mathcal{S}=0}^{\infty} (\mathcal{S} + \mathcal{S}_{\min})^{-\tau}. \quad (11)$$

The corresponding *complementary cumulative distribution function* (cCDF) then reads:

$$\mathcal{F}(\mathcal{S}) = \sum_{\mathcal{S}'=\mathcal{S}}^{\infty} p(\mathcal{S}') = \frac{\zeta(\tau, \mathcal{S})}{\zeta(\tau, \mathcal{S}_{\min})}. \quad (12)$$

Using the numerically computed cCDF (see Appendix XID for methods), we determine the Fisher exponent τ and the lower bound \mathcal{S}_{\min} by employing the Kolmogorov-Smirnov (KS) method [80–82]. In addition to finding the optimal values of τ and \mathcal{S}_{\min} , the KS method assesses how well the power-law model fits and

compares it with other long-tailed distributions. Details on the implementation of the KS method are provided in Appendix XII.

Initially, we apply the KS method to the cluster size distributions for λ values in the vicinity of λ_P . In this range, the logistic GOL ‘unlocks’ dynamic control over cluster behavior, enabling precise tuning of the tail fatness in the cluster distribution through λ . As shown in Fig. 5a, the tail of the cCDFs undershoots the power-law line when $\lambda < \lambda_P$. As λ increases, the number of zero clusters and the variance of cluster sizes increase, resulting in a fatter tail (Fig. 5b). However, at $\lambda = \lambda_P$, we observe that the tail fits with a power law with exponential cutoff (Fig. 5b). This cutoff is due to finite-size effects shown in Fig. 15. Further increases in λ lead to the loss of perfect linearity of the cluster size distribution (Fig. 5c), supporting the assertion that λ_P is the critical point for the emergence of giant clusters. Beyond this point, the largest vacuum cluster separates from the rest of the distribution and begins to percolate. As \mathcal{S}_1 grows to be comparable to the system size N^2 , it diverges from the main body of the distribution (arrow in Fig. 5d). Note that this evolution is also illustrated through simulation snapshots in Fig. 4a.

The fit results of the KS method for cluster distribution at $\lambda = \lambda_P$ yield a power-law distribution with exponential cutoff, with the following coefficients:

$$\lambda_P = 0.86055 : \begin{cases} \tau = 1.81 \pm 0.03 \\ \mathcal{S}_{\min} = 560 \pm 150 \end{cases} \quad (13)$$

The plausibility of the optimal power-law fit to the numerical data is confirmed by the KS method. Additionally, a second test using the KS method assesses whether alternative fat-tailed distributions (*e.g.*, exponential, stretched exponential, or log-normal) offer a better fit than the power law. As shown in Table II, Appendix, the power-law distribution with an exponential cutoff best characterizes the system at λ_P .

Next, we discuss the cluster size distributions in the vicinity of λ_A . As previously mentioned, in this range the lattice is dominated by the largest vacuum cluster. However, we find that the distribution of all other smaller clusters exhibits interesting behavior. Hence, when applying the KS method to the cluster size distributions near λ_A , we always neglect the largest cluster by ‘trimming’ out the separated part of the distribution (arrow in Fig. 5).

As λ approaches λ_A from below, the trimmed cluster size distribution displays similar behavior as in the vicinity of λ_P (Fig. 6). As shown in Fig. 6a,b, the tail begins to approach the power-law line from below. At $\lambda = \lambda_A$, the cluster size distribution follows a power law (Fig. 6c) which, in contrast to the previous case, does not have an exponential cutoff. Then, as λ increases above λ_A , the system transitions to an inactive phase, resulting in the disappearance of cluster dynamics (Fig. 6d). The corresponding power law parameters fitted by the KS method

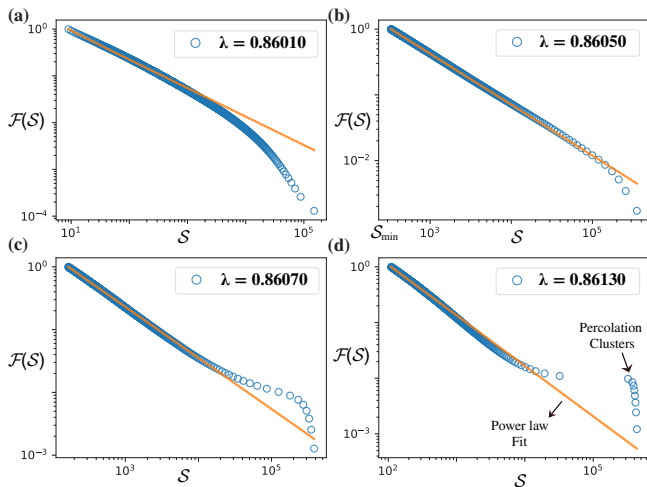


FIG. 5. **The evolution of cluster size distribution around $\lambda_P = 0.86055$.** The empirical complementary cumulative distribution function (cCDF) with *logarithmic-binning* [80] is shown in blue, with the fitted power-law in orange, for λ values (a) below, (b) close and (c)(d) above λ_P . The x-axis starts from the optimal \mathcal{S}_{\min} determined by the KS method (see text). The cluster size distribution becomes a power law (with exponential cutoff) only very close to the critical point λ_P .

read:

$$\lambda_A = 0.8750 : \begin{cases} \tau = 2.9 \pm 0.1 \\ \mathcal{S}_{\min} = 11 \pm 3 \end{cases} . \quad (14)$$

Similarly to the previous case, the comparison test details for λ_A are provided in Appendix Table II.

Further statistical analyses using the KS method over different parameter values in the range $0.8 < \lambda < 0.9$ are discussed in Appendix XII C, where we evaluate the quality of the power-law fits for the cluster size distributions near the critical points. The results of these statistical analyses indicate that:

- At $\lambda_P = 0.86055$, the tail of cluster size distribution follows a power law with exponential cutoff.
- At $\lambda_A = 0.8750$, the tail of cluster size distribution follows a pure power law when the giant vacuum cluster is disregarded.

The different natures of criticality at λ_P and λ_A points are also reflected in their Fisher exponents, τ . At $\lambda = \lambda_P$, where $1 < \tau < 2$, all moments diverge, including the mean $\langle \mathcal{S}(\lambda_P) \rangle$. This arises because percolation-like behavior causes the bulk of the distribution to be highly concentrated in the tail. In the thermodynamic limit, the tail of the distribution (Fig. 5c) extends to infinity, resulting in $\langle \mathcal{S}(\lambda_P) \rangle \rightarrow \infty$. In contrast, at $\lambda = \lambda_A$, where $2 < \tau < 3$, the mean remains finite, and only the variance and higher moments diverge. This means that, unlike λ_P , the critical behavior at λ_A does not constitute of clusters

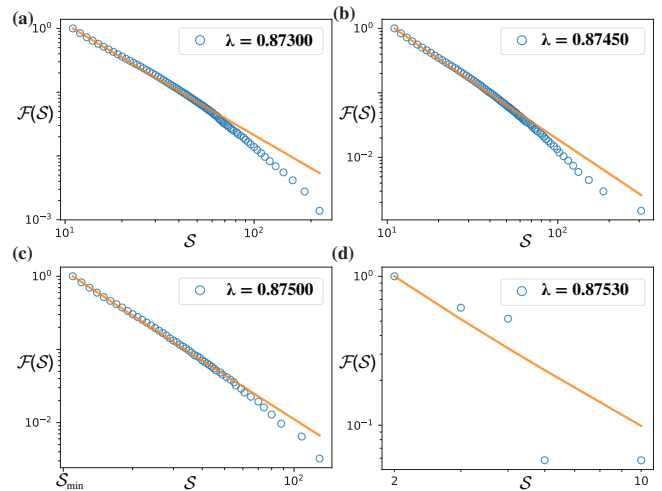


FIG. 6. **The evolution of cluster size distribution around $\lambda_A = 0.8750$, when the largest vacuum cluster is disregarded.** The cCDFs with logarithmic-binning shown in blue, with the fitted power law in orange. The largest vacuum clusters are ignored here and the x-axis starts from the optimal \mathcal{S}_{\min} determined by KS method. The distribution evolves near λ_P by approaching a power law from below and becomes a power law near λ_A . For $\lambda > \lambda_A$, asymptotic activity and cluster formation cease, leading to the disappearance of cluster dynamics.

comparable to the system size. Below, we discuss on the potential mechanisms involved in the emergence of such power-law distributions.

The mechanism behind the percolation transition can be explained as follows. As λ approaches λ_P from below, the system promotes more zero states because several neighborhood sums increase from $m \leq t_3$ to $m > t_3$, inducing decay instead of growth (Section III). As a consequence, clusters of quiescent states grow continuously with λ until they merge with each other at $\lambda = \lambda_P$. In this respect, the dominance of zero states in the grid and the power law behavior of cluster sizes indicates that λ_P marks the point of a deterministic percolation transition. We moreover note that the cluster size distribution exponent $\tau \simeq 1.81$ found in λ_P is lower than exponents in classical 2D ordinary percolation models ($\tau > 2$), hence the universality class of this transition remains unclear. However, we also note that extremely similar exponents have been observed in interesting scenarios, such as the no-enclave percolation model [83] and the percolation of sites not visited by a 2D random walk [84].

The mechanism for the emergence of power law around λ_A is fundamentally different from λ_P . Here, the system is dominated by a vacuum cluster of quiescent states that serves as a ‘playground’ for activity with diverging susceptibility. This susceptible activity spreads in a particular fashion such that it ‘encircles’ quiescent regions in the grid, giving rise to smaller zero-state clusters (Fig. 7). Interestingly, the size of these zero-state clusters encircled by activity follows a power-law distribution, which

emerges close to λ_A . Beyond this value, the power-law ceases because the asymptotic activity stops due to more neighborhood sums inducing decay instead of growth.

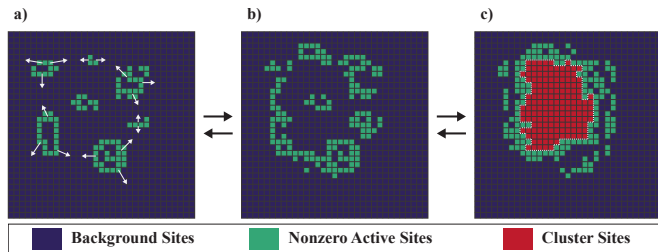


FIG. 7. **A peculiar form of self-organized criticality in the vicinity of λ_A .** As λ approaches λ_A from below, the active nonzero cells move in a manner (a) that occasionally encircles the zero-state background cells (b), forming clusters (c) that give rise to the associated power law. These steps are two-way: just as clusters are formed, they can also fragment in the same manner.

We believe that the power-law behavior in the vicinity of λ_A reflects a form of self-organized criticality (SOC), similar to the one discussed by Bak *et al.* [59][60]. In these studies, it was shown that the activity clusters follow a power law when the asymptotic state of Conway’s GOL is continually perturbed by altering single sites. In our case, the power-law distribution of zero clusters occurs at multiple points in the vicinity of $\lambda < \lambda_A$ (inset of Fig. 16 in Appendix XII C), suggesting scale invariance over a continuous parameter range, similar to the SOC behavior. We speculate that, around λ_A , the logistic GOL administers ‘perturbations’ to itself continually via neighborhood configurations of $m = 4\lambda$ and $m = 5 - 4\lambda$ (Fig. 3). Such configurations seem to be occurring frequently enough to maintain a persistent activity in the lattice through cascades of nearby state changes, thereby generating activity profiles that propagate throughout the lattice. Such activity shares similar nonlinearity with Conway’s GOL, but in contrast, it is persistent without the need of any external perturbations. In this context, Per Bak’s system operates in a ‘stimulated’ SOC regime, while our system functions in a ‘spontaneous’ SOC regime.

VI. DISCUSSION

The logistic GOL is a deterministic variation that alters the dynamics of Conway’s GOL through a single parameter (λ) that tunes the rate at which sites decay/grow in every iteration [53]. Depending on λ , the previously binary state space extends into a Cantor set and the dynamics of the logistic GOL becomes fundamentally different from that of the Conway’s GOL.

In this work, we investigate in detail the asymptotic dynamics of the system and identify at least three distinct dynamical regimes separated by two critical deterministic phase transitions. In the first one (phase I),

where $\lambda_A = 0.8750 < \lambda \leq 1$, the asymptotic dynamics of the logistic GOL is virtually the same as Conway’s GOL, with long transients that eventually settle to sparse populations of stable/oscillating structures in a spanning vacuum cluster of quiescent states [70]. The second dynamical regime (phase II) lies between $\lambda_P = 0.86055 < \lambda \leq \lambda_A$, where the logistic GOL becomes asymptotically active - *i.e.* the dynamics persists in the thermodynamic limit - but still with a vacuum cluster that spans the lattice. As λ is decreased further, activity increases and the size of the vacuum cluster is consequently reduced. The size of this cluster decreases with λ until it disconnects into smaller clusters at λ_P . This second transition defines the limit of the third dynamical regime (phase III), $\lambda \leq \lambda_P$ where the logistic GOL is active and there is no vacuum cluster spanning the lattice.

We use numerical tools from percolation theory to study the dynamics of largest clusters close to the critical point (λ_P) separating phases II and III, and find for the first time a deterministic percolation transition hidden in the Game of Life. We believe that there are two aspects that make this transition interesting. First, the study of percolation transitions – which are widespread in models of physics, networks, and population dynamics – is particularly uncommon in systems where clusters are generated by a purely deterministic process. We are only aware of a few spatially extended systems where transitions from homogeneous to chaotic behavior has been compared to directed percolation processes [85–87]. Second, the cluster size distribution at $\lambda = \lambda_P$ has a Fisher exponent of $\tau \simeq 1.81 < 2$, which is also not typical for percolating systems, except for a few disputed cases [83, 84]. We use numerical tools from percolation theory to study the dynamics of largest clusters close to the critical point (λ_P) separating phases II and III, and find for the first time a deterministic percolation transition hidden in the Game of Life. We believe that there are two aspects that make this transition interesting. First, the study of percolation transitions – which are widespread in models of physics, networks, and population dynamics – is particularly uncommon in systems where clusters are generated by a purely deterministic process. We are only aware of a few spatially extended systems where transitions from homogeneous to chaotic behavior has been compared to directed percolation processes [85–87]. Second, the cluster size distribution at $\lambda = \lambda_P$ has a Fisher exponent of $\tau \simeq 1.81 < 2$, which is also not typical for percolating systems, except for a few disputed cases [75, 83, 84].

Moreover, we study the system in the vicinity of transition between phases I and II, and find that λ_A marks the transition point between these phases. We find that this transition is defined by a discontinuity in the asymptotic activity, and is not related to any cluster merging process. However, we observe that the activity profiles near the border of the active asymptotic phase, *i.e.* when $\lambda \rightarrow \lambda_A^-$, give rise to clusters of zero-states that follow a

power-law distribution (Fig. 7). We believe that this behavior reflects a peculiar form of self-organized criticality, and that it is related to the one observed in early studies of Conway's GOL [59, 60].

VII. CODE AVAILABILITY

The codes used in this research are publicly accessible at <https://github.com/HakanAkgn/ClusterAnalyzer>. This repository offers a library for studying cluster dynamics, and we also encourage its application in other systems.

VIII. ACKNOWLEDGEMENTS

S.J. acknowledges the computing services provided by UHEM. H.A. acknowledges funding and support from the Agency for Science, Technology and Research (A*STAR) through the SIPGA fellowship, the Scientific and Technological Research Council of Türkiye (TÜBİTAK) under TÜBİTAK 2205, and Bilkent University through the Comprehensive Scholarship.

-
- [1] G. Ódor, Universality classes in nonequilibrium lattice systems, *Reviews of Modern Physics* **76**, 663 (2004).
- [2] S. Lübeck, Universal scaling behavior of non-equilibrium phase transitions, *International Journal of Modern Physics B* **18**, 3977 (2004).
- [3] M. Marcuzzi, E. Levi, W. Li, J. Garrahan, and I. Lesanovsky, Non-equilibrium universality in the dynamics of dissipative cold atomic gases, *New Journal of Physics* **17**, 072003 (2015).
- [4] H. Hinrichsen, Non-equilibrium phase transitions, *Physica A: Statistical Mechanics and its Applications* **369**, 1 (2006).
- [5] M. Karl, B. Nowak, and T. Gasenzer, Tuning universality far from equilibrium, *Scientific Reports* **3**, 2394 (2013).
- [6] R. Arouca, C. Lee, and C. M. Smith, Unconventional scaling at non-hermitian critical points, *Physical Review B* **102**, 245145 (2020).
- [7] S. Rafi-Ul-Islam, Z. Siu, H. Sahin, C. Lee, and M. Jalil, Critical hybridization of skin modes in coupled non-hermitian chains, *Physical Review Research* **4**, 013243 (2022).
- [8] J. L. Cardy, Critical percolation in finite geometries, *Journal of Physics A: Mathematical and General* **25**, L201 (1992).
- [9] P. Mathieu and D. Ridout, From percolation to logarithmic conformal field theory, *Physics Letters B* **657**, 120 (2007).
- [10] S. Mertens and C. Moore, Continuum percolation thresholds in two dimensions, *Physical Review E* **86**, 061109 (2012).
- [11] N. Javerzat and M. Bouzid, Evidences of conformal invariance in 2d rigidity percolation, *Physical Review Letters* **130**, 268201 (2023).
- [12] N. Javerzat, Schramm-loewner evolution in 2d rigidity percolation, *Physical Review Letters* **132**, 018201 (2024).
- [13] M. Yang and C. H. Lee, Percolation-induced pt symmetry breaking, *Physical Review Letters* **133**, 136602 (2024).
- [14] D. Stauffer, Scaling theory of percolation clusters, *Physics Reports* **54**, 1 (1979).
- [15] J. W. Essam, Percolation theory, *Reports on Progress in Physics* **43**, 833 (1980).
- [16] C.-K. Hu, Percolation, clusters, and phase transitions in spin models, *Physical Review B* **29**, 5103 (1984).
- [17] R. Parshani, S. V. Buldyrev, and S. Havlin, Interdependent networks: Reducing the coupling strength leads to a change from a first to second order percolation transition, *Physical Review Letters* **105**, 048701 (2010).
- [18] G. Lemoult, L. Shi, K. Avila, S. V. Jalikop, M. Avila, and B. Hof, Directed percolation phase transition to sustained turbulence in couette flow, *Nature Physics* **12**, 254 (2016).
- [19] H. Hinrichsen, Non-equilibrium critical phenomena and phase transitions into absorbing states, *Advances in Physics* **49**, 815 (2000).
- [20] A. V. Goltsev, S. N. Dorogovtsev, and J. F. F. Mendes, k-core (bootstrap) percolation on complex networks: Critical phenomena and nonlocal effects, *Physical Review E* **73**, 056101 (2006).
- [21] S. N. Dorogovtsev, A. V. Goltsev, and J. F. F. Mendes, Critical phenomena in complex networks, *Reviews of Modern Physics* **80**, 1275 (2008).
- [22] S. Kim, T. Senthil, and D. Chowdhury, Continuous mott transition in moiré semiconductors: role of long-wavelength inhomogeneities, *Physical Review Letters* **130**, 066301 (2023).
- [23] C. Müller, M. H. Müser, G. Carbone, and N. Menga, Significance of elastic coupling for stresses and leakage in frictional contacts, *Physical Review Letters* **131**, 156201 (2023).
- [24] J. Wang, D. Liu, L. Yu, F. Liu, J. Niu, G. Yang, C. Lu, N. Lu, L. Li, and M. Liu, Collective transport for nonlinear current-voltage characteristics of doped conducting polymers, *Physical Review Letters* **130**, 177001 (2023).
- [25] S. Das and S. Biswas, Critical scaling through gini index, *Physical Review Letters* **131**, 157101 (2023).
- [26] X. Meng, J. Gao, and S. Havlin, Concurrence percolation in quantum networks, *Physical Review Letters* **126**, 170501 (2021).
- [27] A. Deger, A. Lazarides, and S. Roy, Constrained dynamics and directed percolation, *Physical Review Letters* **129**, 190601 (2022).
- [28] K. Krishnaraj and P. R. Nott, Coherent force chains in disordered granular materials emerge from a percolation of quasilinear clusters, *Physical Review Letters* **124**, 198002 (2020).
- [29] L. Falsi, M. Aversa, F. Di Mei, D. Pierangeli, F. Xin, A. J. Agranat, and E. DelRe, Direct observation of fractal-dimensional percolation in the 3d cluster dynamics of a ferroelectric supercrystal, *Physical Review Letters* **126**, 037601 (2021).

- [30] Y. Wang, S. Fang, N. Xu, and Y. Deng, Two-scale scenario of rigidity percolation of sticky particles, *Physical Review Letters* **124**, 255501 (2020).
- [31] A. Lavasani, Y. Alavirad, and M. Barkeshli, Topological order and criticality in (2+1)d monitored random quantum circuits, *Physical Review Letters* **127**, 235701 (2021).
- [32] G. Peng, Invasion percolation in deterministic systems, *Physical Review Letters* **64**, 1346 (1990).
- [33] J. Clerc, G. Giraud, J. Laugier, and J. Luck, Electrical responses in deterministic fractal networks, *Journal of Physics A: Mathematical and General* **21**, 1703 (1988).
- [34] L. Limat, J. Clerc, G. Giraud, J. Laugier, and J. Luck, Elastic responses in deterministic fractal networks, *Physical Review B* **37**, 354 (1988).
- [35] C. H. Lee, D. Ozaki, and H. Matsueda, Random-fractal ansatz for the configurations of two-dimensional critical systems, *Physical Review E* **94**, 062144 (2016).
- [36] C. A. S. Tercariol and C. P. C. Prado, Critical transitions in deterministic walks and sandpile models, *Physica A: Statistical Mechanics and its Applications* **373**, 199 (2007).
- [37] H. Bhaumik and R. Pandit, Critical properties of deterministic and stochastic sandpile models on two-dimensional percolation backbone, *Communications in Mathematical Physics* **207**, 43 (1999).
- [38] I. Vardi, Deterministic percolation, *Communications in Mathematical Physics* **207**, 43 (1999).
- [39] I. Vardi, Deterministic bootstrap percolation on trees, *The Art of Discrete and Applied Mathematics* **4**, 20c (2021).
- [40] M. Gardner, Mathematical games: The fantastic combinations of john conway’s new solitaire game ‘life’, *Scientific American* **223**, 120 (1970).
- [41] E. M. Izhikevich, J. H. Conway, and A. Seth, Game of Life, *Scholarpedia* **10**, 1816 (2015), revision #150735.
- [42] E. R. Berlekamp, J. H. Conway, and R. K. Guy, *Winning ways for your mathematical plays, volume 4* (AK Peters/CRC Press, 2004).
- [43] P. W. Rendell, A universal turing machine in conway’s game of life, *2011 International Conference on High Performance Computing & Simulation*, 764 (2011).
- [44] R. D. Beer, The Cognitive Domain of a Glider in the Game of Life, *Artificial Life* **20**, 183 (2014), <https://direct.mit.edu/artl/article-pdf/20/2/183/1664518/artl.a.00125.pdf>.
- [45] P. D. Turney, Evolution of Autopoiesis and Multicellularity in the Game of Life, *Artificial Life* **27**, 26 (2021), <https://direct.mit.edu/artl/article-pdf/27/1/26/2020415/artl.a.00334.pdf>.
- [46] N. H. Packard and J. S. McCaskill, Open-Endedness in Genelife, *Artificial Life* **30**, 356 (2024), <https://direct.mit.edu/artl/article-pdf/30/3/356/2462580/artl.a.00426.pdf>.
- [47] N. Brown, C. Cheng, T. Jacobi, M. Karpovich, M. Merzenich, D. Raucci, and M. Riley, *Conway’s game of life is omniperiodic* (2023), [arXiv:2312.02799 \[math.CO\]](https://arxiv.org/abs/2312.02799).
- [48] W. Gilpin, Cellular automata as convolutional neural networks, *Phys. Rev. E* **100**, 032402 (2019).
- [49] D. A. Faux and P. Bassom, The game of life as a species model, *American Journal of Physics* **91**, 561 (2023), https://pubs.aip.org/aapt/ajp/article-pdf/91/7/561/20105275/561_1_5.0150858.pdf.
- [50] T. Kawano, Translating the conway game of life as a discrete logistic cellular automata model with density effects, *International Journal of Innovative Computing, Information and Control* **16**, 1655 (2020).
- [51] J. H. Rainwater, Self-Organization and Phase Transitions in Driven Cellular Automata, *Artificial Life* **30**, 302 (2024), <https://direct.mit.edu/artl/article-pdf/30/3/302/2462558/artl.a.00437.pdf>.
- [52] A. Adamatzky, *Game of life cellular automata*, Vol. 1 (Springer, 2010).
- [53] M. Ibrahim, O. Gülseren, and S. Jahangirov, Deterministic phase transitions and self-organization in logistic cellular automata, *Phys. Rev. E* **100**, 042216 (2019).
- [54] K. M. Evans, Larger than life: threshold-range scaling of life’s coherent structures, *Physica D: Nonlinear Phenomena* **183**, 45 (2003).
- [55] P. Arrighi and J. Grattage, The quantum game of life, *Physics World* **25**, 23 (2012).
- [56] P.-M. Ney, S. Notarnicola, S. Montangero, and G. Morigi, Entanglement in the quantum game of life, *Phys. Rev. A* **105**, 012416 (2022).
- [57] R. Banerjee and T. C. H. Liew, Artificial life in an exciton-polariton lattice, *New Journal of Physics* **22**, 103062 (2020).
- [58] O. Liolis, G. C. Sirakoulis, and A. Adamatzky, Conway’s game of life in quantum-dot cellular automata, *Microelectronics Journal* **109**, 104972 (2021).
- [59] P. Bak, K. Chen, and M. Creutz, Self-organized criticality in the ‘game of life’, *Nature* **342**, 780 (1989).
- [60] P. Alstrøm and J. a. Leão, Self-organized criticality in the “game of life”, *Phys. Rev. E* **49**, R2507 (1994).
- [61] J. Hemmingsson, Consistent results on ‘life’, *Physica D: Nonlinear Phenomena* **80**, 151 (1995).
- [62] H. J. Blok and B. Bergersen, Synchronous versus asynchronous updating in the “game of life”, *Phys. Rev. E* **59**, 3876 (1999).
- [63] A. P. Vieira, E. Goles, and H. J. Herrmann, Phase transitions in a conservative game of life, *Phys. Rev. E* **103**, 012132 (2021).
- [64] L. S. Schulman and P. E. Seiden, Statistical mechanics of a dynamical system based on conway’s game of life, *Journal of Statistical Physics* **19**, 293 (1978).
- [65] J. Nordfalk and P. Alstrøm, Phase transitions near the “game of life”, *Phys. Rev. E* **54**, R1025 (1996).
- [66] R. A. Monetti and E. V. Albano, Critical edge between frozen extinction and chaotic life, *Phys. Rev. E* **52**, 5825 (1995).
- [67] S.-Y. Huang, X.-W. Zou, Z.-J. Tan, and Z.-Z. Jin, Network-induced nonequilibrium phase transition in the “game of life”, *Phys. Rev. E* **67**, 026107 (2003).
- [68] S. M. Reia and O. Kinouchi, Conway’s game of life is a near-critical metastable state in the multiverse of cellular automata, *Physical Review E* **89**, 052123 (2014).
- [69] K. Ito and Y.-P. Gunji, Self-organization toward criticality in the game of life, *Biosystems* **26**, 135 (1992).
- [70] F. Bagnoli, R. Rechtman, and S. Ruffo, Some facts of life, *Physica A: Statistical Mechanics and its Applications* **171**, 249 (1991).
- [71] J. B. C. Garcia, M. A. F. Gomes, T. I. Jyh, T. I. Ren, and T. R. M. Sales, Nonlinear dynamics of the cellular-automaton ‘game of life’, *Phys. Rev. E* **48**, 3345 (1993).
- [72] W. K. Wootters and C. G. Langton, Is there a sharp phase transition for deterministic cellular automata?, *Physica D: Nonlinear Phenomena* **45**, 95 (1990).

- [73] M. Ibrahimi, A. Güçlü, N. Jahangirov, M. Yaman, O. Gülseren, and S. Jahangirov, Operator representation and class transitions in elementary cellular automata, *Complex Systems* **31**, 415 (2022).
- [74] R. M. May, Simple mathematical models with very complicated dynamics, *Nature* **261**, 459 (1976).
- [75] H. Hu, R. M. Ziff, and Y. Deng, No-enclave percolation corresponds to holes in the cluster backbone, *Phys. Rev. Lett.* **117**, 185701 (2016).
- [76] D. Stauffer and A. Aharony, *Introduction to Percolation Theory*, 2nd ed. (CRC Press, London, 1994) Chap. 2.8.
- [77] M. Sahimi, *Applications of Percolation Theory* (Taylor & Francis, London, 1994) p. 154.
- [78] M. Newman, *Networks* (Oxford University Press, 2018) chapter 11.6.
- [79] M. E. Fisher, The theory of condensation from a lattice gas, *Physical Review A* **4**, 658 (1969).
- [80] A. Clauset, C. R. Shalizi, and M. E. Newman, Power-law distributions in empirical data, *SIAM review* **51**, 661 (2009).
- [81] J. Alstott, E. Bullmore, and D. Plenz, powerlaw: A Python Package for Analysis of Heavy-Tailed Distributions, *PLoS ONE* **9**, e85777 (2014).
- [82] A.-L. Barabási, Network science, *Philosophical Transactions of the Royal Society A: Mathematical, Physical and Engineering Sciences* **371**, 20120375 (2013).
- [83] M. Sheinman, A. Sharma, J. Alvarado, G. H. Koenderink, and F. C. MacKintosh, Anomalous discontinuity at the percolation critical point of active gels, *Phys. Rev. Lett.* **114**, 098104 (2015).
- [84] A. Federbush and Y. Kantor, Percolation perspective on sites not visited by a random walk in two dimensions, *Phys. Rev. E* **103**, 032137 (2021).
- [85] H. Chate and P. Manneville, Spatio-temporal intermittency in coupled map lattices, *Physica D: Nonlinear Phenomena* **32**, 409 (1988).
- [86] P. Grassberger and T. Schreiber, Phase transitions in coupled map lattices, *Physica D: Nonlinear Phenomena* **50**, 177 (1991).
- [87] Y. Cuche, R. Livi, and A. Politi, Phase transitions in 2d linearly stable coupled map lattices, *Physica D: Nonlinear Phenomena* **103**, 369 (1997), lattice Dynamics.
- [88] R. E. Tarjan, Efficiency of a good but not linear set union algorithm, *Journal of the ACM* **22**, 215 (1975).
- [89] A. H. Land and A. G. Doig, An automatic method of solving discrete programming problems, *Econometrica* **28**, 497 (1960).
- [90] K. Christensen and N. R. Moloney, *Complexity and Criticality* (Imperial College Press, London, 2005) section 1.7.2, *Mass of a large but finite cluster at $p = p_c$* .
- [91] D. Stauffer and A. Aharony, *Introduction to Percolation Theory* (Taylor & Francis, London, 1994) pp. Section 3.4, "The Infinite Cluster at the Threshold".
- [92] Q. H. Vuong, Likelihood ratio tests for model selection and non-nested hypotheses, *Econometrica: journal of the Econometric Society* , 307 (1989).

Methods

IX. TRUNCATION OF THE STATE SPACE AND IMPLEMENTATION OF THE LOGISTIC GOL

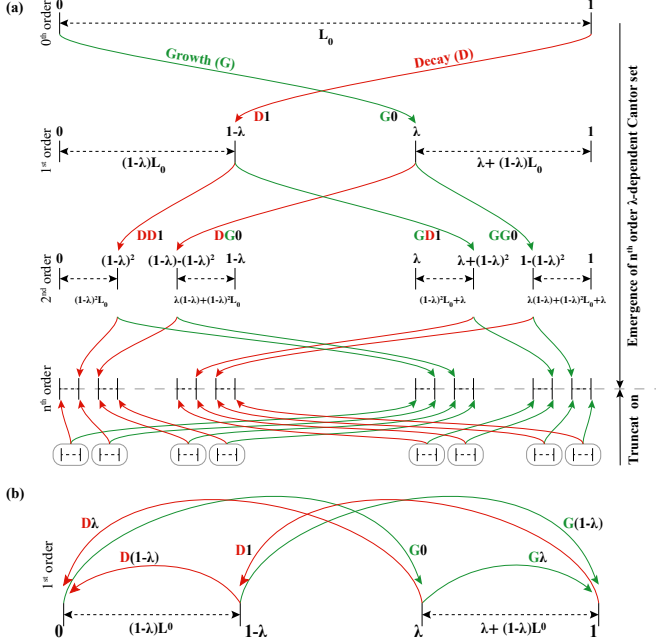


FIG. 8. **State space across different orders and truncation process.** (a) The state space in the logistic GOL expands into a Cantor set, where the dissection ratio is set by λ . Different levels show the emergence of the first two orders of the Cantor set from applying the rules to a uniform distribution. In this study, we truncate the state space at a finite order to analyze the cluster dynamics of the system. (b) The decay and growth operations for the first order are illustrated in the truncated space. The truncation preserves the operational regimes, and lumping nearby states allows for maintaining the same dynamic behavior as the logistic GOL.

Starting from the logistic GOL, we retain only the Cantor set up to order n , truncating the rest. The state space is discretized into $L_n = 2^{n+1}$ states, which are generated recursively as follows:

$$L = \begin{cases} L_0 = \{0, 1\} \\ L_1 = \{0, 1 - \lambda, \lambda, 1\} \\ L_2 = \{0, (1 - \lambda)^2, \dots, 1 - (1 - \lambda)^2, 1\} \\ \vdots \\ L_n = (1 - \lambda)L_{n-1} \cup (L_{n-1}(1 - \lambda) + \lambda) \end{cases}$$

The set L_n represents all possible combinations of growth and decay operations on the initial set $L_0 = \{0, 1\}$. To ensure the preservation of the number of states, the map the state space onto itself:

$$s_j^{t+1} = \begin{cases} \mathbf{S}s_j^t \equiv s_j^t & \text{if } t_1 \leq m_j^t < t_2, \\ \mathbf{G}s_j^t \equiv M_{L_n}((1 - \lambda)s_j^t + \lambda) & \text{if } t_2 \leq m_j^t < t_3, \\ \mathbf{D}s_j^t \equiv M_{L_n}((1 - \lambda)s_j^t) & \text{otherwise.} \end{cases} \quad (15)$$

where M_{L_n} is defined as the nearest-element projection onto L_n :

$$M_{L_n}(x) = \arg \min_{y \in L_n} |x - y|$$

This setup with M_{L_n} ensures that each transformed state is mapped to the nearest valid state within L_n , preserving the structure and permutation of the state space. The evolution and truncation of state spaces across different orders are illustrated in Fig. 8a.

The operational domains remain the same throughout the truncation process, but now the range of Moore sum m is discretized instead of being continuous. The growth/decay operations for the first-order truncation are illustrated in Fig. 8b. As the order n tends to infinity, the truncated version approaches the continuous state space of the logistic GOL. We note here that, when performing numerical simulations, the state space is nevertheless truncated in some order depending on the numerical resolution of the implementation program.

Employing the truncated version of the logistic GOL, we run $n = 10$ order simulations on a 1000×1000 grid under periodic boundary conditions (PBC). For each simulation, we discard the burn-in period of 10^5 time steps to ensure the system reaches equilibrium and then average over the next 10^5 time steps. For each λ , we run 5000 simulations and then average over the ensembles. Clusters and their sizes are obtained by connecting adjacent cells that are in the same state, realized by the *union-find* algorithm [88]. All the expected values of observables (activity, susceptibility, cluster sizes, etc.) are acquired by time-averaging and ensemble-averaging the raw data.

X. EXPLICIT NEIGHBORHOOD OF PERCOLATION TRANSITION λ_P

To approximate a target value, the algorithm selects a subset of Cantor set states that sum closely to the desired target within a specified tolerance. This is achieved using a branch-and-bound approach [89], which explores possible combinations of states while discarding unpromising paths. In this approach, the algorithm iteratively builds subsets of the Cantor set by adding states and checking if the current sum is within tolerance. The process is optimized by pruning paths that cannot meet the target, based on the following criteria:

- **Subset Size Constraint:** Paths that exceed the allowed number of states are discarded.

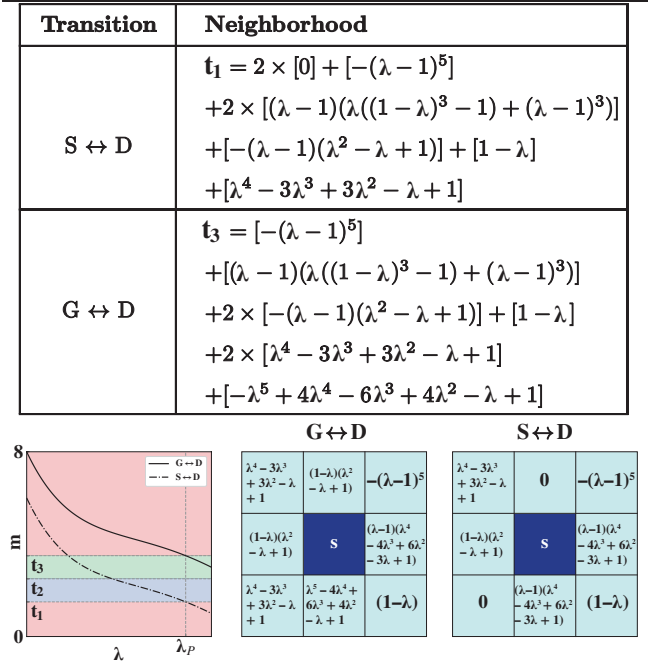


FIG. 9. **Explicit operational transitions for λ_P** The table above presents the fifth-order λ neighborhood transitions for the t_1 and t_3 neighborhoods at λ_P . The panel below shows neighborhoods undergoing transition, while the lower left panel illustrates the numerical evolution of these neighborhoods as λ varies between $0 < \lambda < 1$.

- **Tolerance Check:** Paths with cumulative sums that deviate from the target by more than the tolerance are also discarded. The tolerance is set to 0.00001 to match the resolution of our numerical simulations.
- **Feasibility Pruning:** The algorithm estimates the minimum and maximum possible sums with remaining states. Paths are pruned if they cannot reach or exceed the target based on these bounds.

This process ensures efficient exploration of feasible subsets, yielding an optimal selection that best approximates the target. Accordingly, Fig. 9 represents the 5th-order Cantor set. As the percolation transition is continuous, approaching the exact percolation point λ_p with high decimal precision requires progressively higher-order neighborhoods. Fig. 3 presents the summed and simplified polynomial representations of these neighborhoods.

XI. NUMERICAL METHODS FOR CLUSTER CHARACTERIZATIONS

A. Box-counting method for the capacity dimension

The box-counting method determines the capacity dimension of an object by covering it with grids of vary-

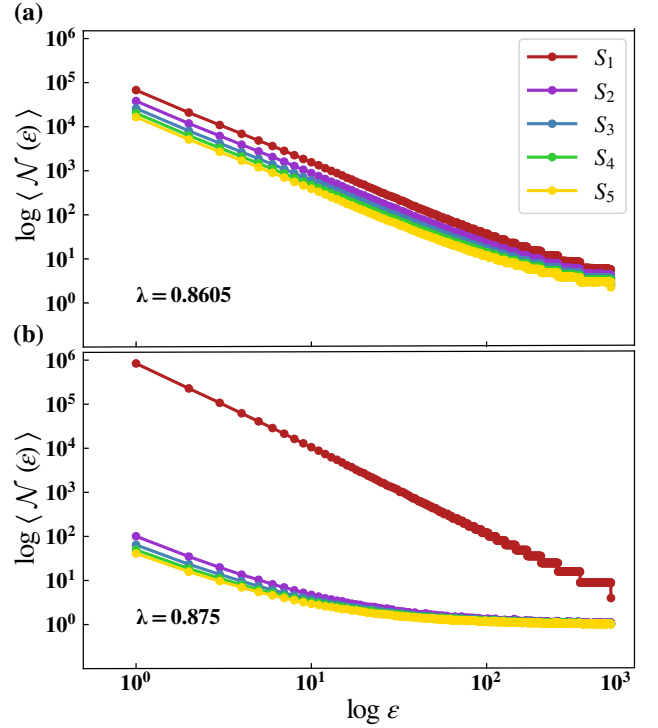


FIG. 10. **The capacity dimension obtained by box-counting.** The plots show the (averaged) box counts $\langle N(\epsilon) \rangle$ v.s. box sizes ϵ , (a) for $\lambda = 0.86$ and (b) for $\lambda = 0.874$. The capacity dimension equals the negative of the slope near $\epsilon = 0$. As λ increases from $\lambda = 0.86$ to $\lambda = 0.874$, the largest cluster gradually separates from the rest, exhibiting an increasing capacity dimension, while the other clusters' capacity dimensions decrease.

ing box sizes and counting the number of boxes, $N(\epsilon)$, that contain part of the object. By analyzing how $N(\epsilon)$ changes with the box size ϵ , the capacity dimension d_c is obtained through the following steps:

1. Cover the cluster with a grid of boxes of size ϵ .
2. Count the minimal number of boxes needed to cover the cluster, denoted as $\mathcal{N}(\epsilon)$.
3. Repeat the steps above over multiple time steps and different initializations to obtain the average box count $\langle \mathcal{N}(\epsilon) \rangle$ for each box size (ϵ).
4. Plot $\log \langle \mathcal{N}(\epsilon) \rangle$ v.s. $\log \epsilon$.
5. Determine the slope of the plot in the small box size region (specifically $\epsilon = [1, 6]$). The capacity dimension d_c is given by:

$$\langle \mathcal{N}(\epsilon) \rangle \propto \epsilon^{-d_c} \quad \rightarrow \quad d_c = - \lim_{\epsilon \rightarrow 0} \frac{\log \langle \mathcal{N}(\epsilon) \rangle}{\log \epsilon}$$

The slopes representing the capacity dimensions of the five largest clusters at two critical points are shown in Fig. 10, highlighting their distinct characteristics. Near

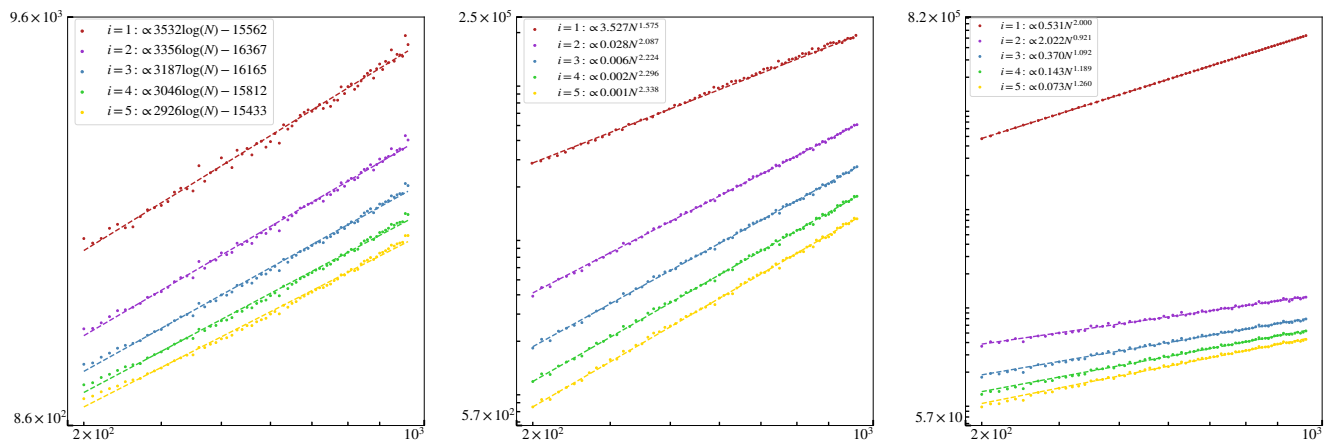


FIG. 11. **Numerical fits of cluster size scaling.** (a) In the subcritical regime ($\lambda < \lambda_P$), cluster sizes $\langle S_i(N) \rangle$ exhibit logarithmic scaling, appearing linear in log-linear plot. (b) At the critical regime ($\lambda \approx \lambda_P$), cluster sizes scale as a power law with system size, indicating the fractal nature of the percolating cluster, appearing linear in log-log plot. (c) In the supercritical regime ($\lambda > \lambda_P$), all subleading clusters $\langle S_i \rangle$ follow logarithmic-like scaling, while the largest cluster $\langle S_1 \rangle$ scales proportionally to the system dimension, appearing linear in log-log plot.

λ_P all clusters have the same slope Fig. 10a, showing increased self-similarity of the system. Above λ_P , the largest cluster's slope increases and becomes more area-like, while other cluster slopes decrease and become more chain-like Fig. 10b. As the largest cluster percolates and fills the entire PBC grid (excluding quiescent states), it forms a two-dimensional surface with $d_c = 2$.

However, it should be noted that the box-counting behavior holds only until the box size reaches the size of the clusters. Similar to other percolation models [90], this relationship can be understood in terms of the mass of a given cluster at the percolation threshold:

$$M(C_i, \lambda_P; \ell) = S_i(\lambda_P; \ell) \propto \begin{cases} \ell^{d_c} & \text{for } \ell \ll R_s, \\ S_i & \text{for } \ell \gg R_s, \end{cases} \quad (16)$$

where $S_i(\lambda_P; \ell)$ is the number of sites in the i -th cluster for a given window length ℓ , which corresponds to the effective box size in the counting process. When ℓ exceeds the characteristic cluster radius R_s , further increasing the window size (i.e., the effective box size) does not capture additional cluster sites; instead, the larger boxes simply encompass the existing sites, leading to no increase in the count of occupied boxes. This is because the cluster is now fully covered, meaning that regardless of additional window size increases, the same number of boxes is needed to cover the entire cluster. This results in a flattening behavior, as seen in Fig. 10b, where smaller clusters are fully covered by a constant number of boxes.

B. The scaling fits and fractal dimension at $\lambda = \lambda_P$

Fig. 11 presents the numerical fits for the scaling of cluster sizes $\langle S_i(N) \rangle$ across different per-

colation regimes. We perform fits on data points for system sizes N from 200 to 1000 in increments of 10. A moderate system size, such as $N = 200$, ensures statistically consistent cluster dynamics across various λ neighborhoods, independent of initial configuration. Since $\lambda = 0.86055$ does not exactly match the analytical percolation point and has additional significant decimal places beyond 0.00001, it is expected that, like other percolation models, system scaling will eventually deviate from a perfect power law [91]. Therefore, as in other percolation models, fits should be performed in the small N regime. Consequently, for our numerical fits, the small N regime [200, 1000] is selected.

Since common neighborhoods tend to decay and become passive in this regime, smaller grid sizes are sufficient for effectively capturing scaling dynamics. For these fits, we specifically use the λ values: $\lambda = 0.855$, $\lambda = 0.86055$, and $\lambda = 0.865$, respectively, for the subcritical, critical, and supercritical regimes.

In the subcritical regime (Fig. 11a), the cluster sizes follow a logarithmic scaling law $\langle S_i(N) \rangle \sim a_i \log N + b_i$, with coefficients a_i and b_i depending on the cluster rank i .

At the critical point λ_P (Fig. 11b), the scaling transitions to a power law, with the largest cluster following $\langle S_1(N) \rangle \sim N^{1.575}$, indicative of the system's fractal nature at criticality. Subleading clusters scale similarly with different exponents. These power-law fits reflect the fractal dimensions of clusters (d_f), a hallmark of critical phenomena. While the largest cluster follows a fractal scaling law, subleading clusters exhibit different exponents as a result of their sensitivity to system size and non-system-spanning nature [15?]. These clusters remain fractal, scaling with exponents indicative of their distribution near criticality. Numerical fits estimate the system's fractal dimension as $d_f \approx 1.575$ with a stan-

standard deviation of $\sigma_f \approx 0.1$, reflecting deviations from the critical point λ_P in simulations. While this result is consistent with expected values near the percolation threshold, slight deviations from the exact critical point may lead to variations in the exponent.

In the supercritical regime (Fig. 11c), the largest cluster $\langle S_1 \rangle$ scales with the system's Euclidean dimension, following a numerical fit of $\langle S_1(N) \rangle \sim N^{1.9997}$, which is very close to the expected N^2 , signaling the emergence of a percolating cluster. Meanwhile, subleading clusters adhere to logarithmic-like scaling, indicating that while they grow with system size, they remain much smaller compared to the largest cluster. This analysis confirms that the scaling behavior of clusters across percolation regimes is consistent with classical percolation models.

C. The second largest cluster peak divergence

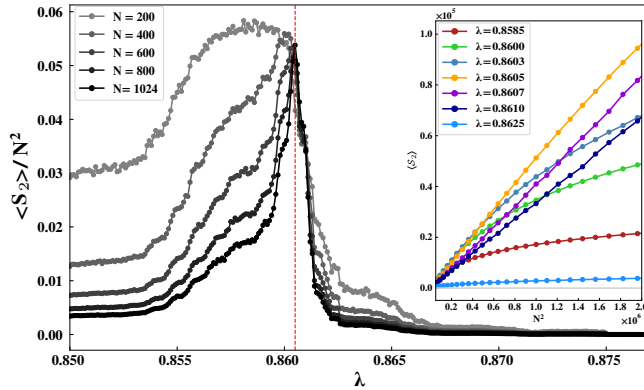


FIG. 12. **Size evolution of the second largest cluster with respect to the system size near λ_P .** As the system approaches the critical point λ_P , the scaling rate of $\langle S_2 \rangle$ increases. As N grows larger, this results in divergence of the peak compared to nearby points. When $\langle S_2 \rangle / N^2$ is plotted this divergence manifests itself as increasing sharpness of the peak.

We examine how $\langle S_2(N) \rangle$ scales with system size N . The simulation was conducted over the range $\lambda \in [0.85, 0.88]$, with increments of 0.001.

It should be again noted that all top-ranking clusters, including $S_2(N)$, are quiescent clusters. As λ_P is approached, the second-largest cluster $\langle S_2(N) \rangle$ grows rapidly, as shown in Fig. 12. At λ_P , it exhibits the fastest divergence, while at nearby points, the growth is slower. In the limit $N \rightarrow \infty$, $\langle S_2 \rangle$ shown in Fig. 4(b) diverges sharply at λ_P , signaling the emergence of a percolating cluster and the phase transition [78]. For brevity, we display only $\langle S_2 \rangle$, but the same behavior and analysis apply to other $\langle S_i \rangle$ peaks. The observed divergence of the second largest cluster peak aligns with the expectations in percolation theory.

D. Cluster size distributions from numerical simulations

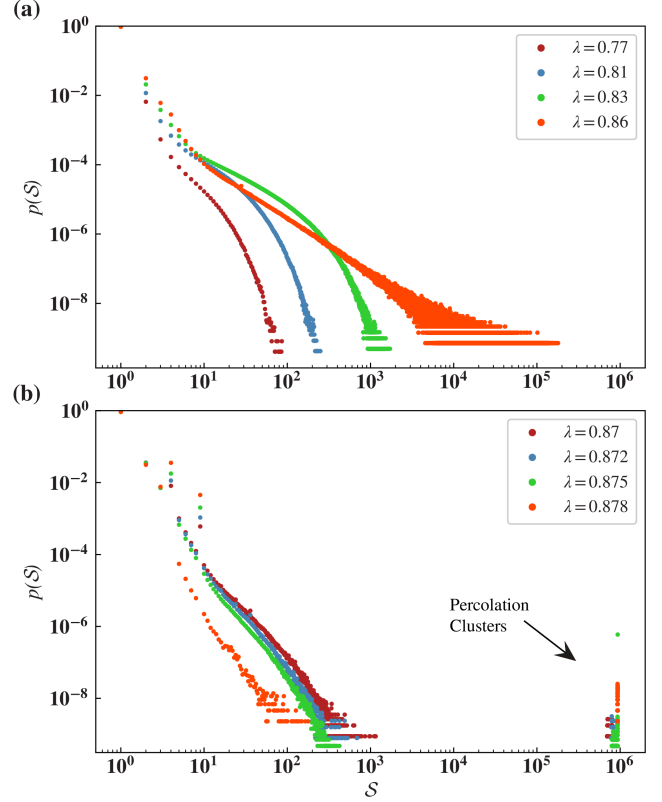


FIG. 13. Log-log plot of the empirical probability density function (PDF) of cluster sizes for different λ values. (a) Evolution of PDFs towards λ_P from below shows that the PDF tails get fatter, both by shifting to higher cluster sizes and increasing the spread of the tail. At λ_P , the tail extends up to the system size, regardless of grid size, indicating scale-invariance. Constrained by the system size, the fitted power-law has an additional exponential cutoff term ($x^{-\tau} e^{-\lambda x}$). (b) Around λ_A , samples of the percolation cluster separate from the rest, piling up away at the end shown with the black arrow. At λ_A , the percolating cluster is discarded before fitting the power law, and the fitted model is a pure power law ($x^{-\tau}$). It doesn't have the cutoff term because only the percolating cluster is affected by the system size.

We present the cluster size distributions near two critical points λ_P and λ_A in Fig. 13. We obtain the numerical count of clusters using the *union-find* algorithm [88], and by normalizing these counts with the total number of clusters, we interpret the data as frequency distributions and treat them as probability density functions (PDFs), denoted by $p(S)$. At $\lambda_P = 0.86055$, the cluster size distribution $p(S)$ seems to follow a power law, while others around it appear as stretched exponentials (Fig. 13a). The piles at the far tail of the distributions around λ_A are contributed by the samples of percolating clusters denoted by the black arrow. After discarding the piles and

truncating the lower curving head, the cluster size distribution at $\lambda_A = 0.875$ also appears to follow a power law (Fig. 13b).

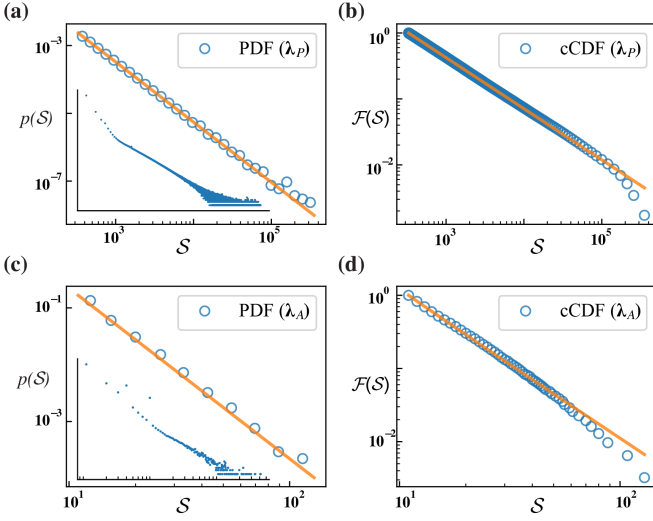


FIG. 14. **The results of KS method at two critical points.** (a)&(c) show PDFs with *logarithmic-binning* and power-law fits by KS methods; the insets show the original PDFs (*linear-binning* and no truncation). (b)&(d) show the corresponding log-binned cCDFs with power-law fits. (a)&(b) are results at λ_P ; (c)&(d) are results at λ_A .

Next, we define the cumulative distribution function (CDF) as the sum of probabilities up to $p(S < s)$, and the complementary cumulative distribution function (cCDF) as $\mathcal{F}(S) = 1 - p(S < s)$. To further reduce statistical fluctuations coming from each individual sample, we apply logarithmic binning, resulting in the plots shown in Fig. 5 and Fig. 6.

Previous studies have demonstrated that applying the Kolmogorov-Smirnov (KS) method to the log-binned cCDF yields more reliable results compared to applying it directly to the raw PDF [80]. This is because the cCDF and log-binning smooths out the statistical fluctuations inherent in raw data, providing a more stable statistical measure. To ensure the robustness of our results, we follow the same methodology here. Fig. 14 demonstrates *log-binned* PDF and cCDFs for λ_P and λ_A . The difference between logarithmic-binning and the conventional linear-binning is that logarithmic-binning divides the data into bins whose widths increase exponentially, which is useful for analyzing data that spans several orders of magnitude. This approach ensures that each bin contains a sufficient number of data points even in the tails of the distribution, thereby reducing noise and providing a clearer representation of the underlying distribution. In contrast, linear-binning divides the data into equally spaced bins, which can lead to sparsity and high statistical fluctuations in regions where data points are scarce, especially when dealing with heavy-tailed distributions. Note that since we set the bins' interval on

log-scaled axis is the same for all plots, distributions with larger domain will have more bins – e.g., Fig. 14b has larger domain $\sim (10^2, 10^6)$ compared to Fig. 14d whose domain $\sim (10^1, 10^3)$, thus Fig. 14b has denser data points.

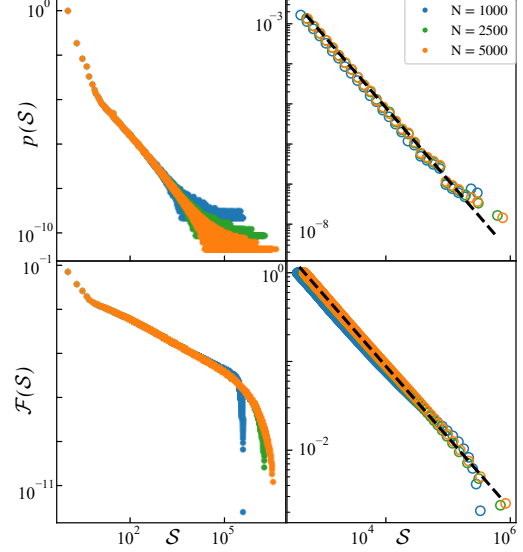


FIG. 15. **Grid size invariance of cluster distributions at critical threshold λ_P .** a shows how the PDFs evolve with increasing grid size (N). As the grid size increases, the tail extends further. b shows the power law fits to log-binned PDFs. It can be seen that, as the grid size evolves, the PDF behavior remains consistent. c shows how the cCDFs evolve with increasing N . The tail extension is directly apparent, and the exponential cutoff term depends on the value of N . d shows the power law fits to log-binned cCDFs. It can be seen that the consistent power-law behavior is preserved across increasing grid sizes, and the optimal fits overlap. The black lines represent the corresponding power-law fits, and for all three sizes, the fits overlap with only slight deviations..

E. Size Evolution of Cluster Distributions at λ_A

For λ_P , Fig. 15 shows that the cluster distribution extends up to the system size regardless of grid size (N). The exponential cutoff appears only due to the system's finite size, with the cutoff point shifting to larger values as N increases. This analysis was not performed for λ_A since criticality at λ_A is not constrained by grid size and its distribution does not extend to the system size. Consistent power-law behavior for λ_P is observed, as indicated by the overlapping on black dashed fit, confirming the presence of percolation behavior. In the power-law relation presented in Eq. 13, we use a grid size of $N = 5000$. For the plots with multiple λ points, we display samples

with a grid size of $N = 1000$ due to computational limitations.

XII. KOLMOGOROV-SMIRNOV METHOD

One important fact about empirical power-law data is that the scaling is rarely valid for the full range of the data. More often, the power law applies only for values greater than some minimum \mathcal{S}_{\min} , i.e., only the *tail* follows a power law. Kolmogorov-Smirnov (KS) method [80–82] is proposed to determine the τ and \mathcal{S}_{\min} , test the *goodness-of-fit*, and compare between alternative fat-tailed models via *Log-likelihood ratio test* in a principled manner.

The optimal \mathcal{S}_{\min} minimizes the relative KS statistic between the empirical data and the fitted model while the optimal τ maximizes the likelihood of the data given the model. However, fitting the data and obtaining $(\tau, \mathcal{S}_{\min})$ alone does not tell us how well the power-law model fits the data; thus, we need a *goodness-of-fit test* that returns a p -value quantifying the plausibility of the power law hypothesis (p_{gf}). The closer p_{gf} is to 1, the more likely it is that the difference between the empirical data and the model can be attributed to statistical fluctuations alone. If p_{gf} is very small, the model is not a plausible fit to the data. Barabási [82, Chap. 4] suggests the model is accepted if $p_{gf} > 0.01$, while Clauset *et al.* [80] proposes a harsher threshold of $p_{gf} > 0.1$. We adopt the latter.

Even if we obtain a plausible power-law fit, it does not guarantee that the power law ($\propto x^{-\tau}$) is the best model. To rigorously assess its suitability, we must compare the power-law model against alternative fat-tailed distributions. Following the approach of Clauset *et al.* [80], we apply the KS method, including the following set of alternatives: power law with exponential cutoff ($\propto x^{-\tau} e^{-\lambda x}$), exponential ($\propto e^{-\lambda x}$), stretched exponential ($\propto x^{\beta-1} e^{-\lambda x^{\beta}}$), and log-normal ($\propto \frac{1}{x} \exp\left[-\frac{(\ln x - \mu)^2}{2\sigma^2}\right]$).

A. KS statistic & KS test

The *Kolmogorov-Smirnov statistic* (KS statistic) measures the distance of two probability distributions. It's able to quantify how *dissimilar* the empirical distribution is from the theoretical distribution / fitted model. Utilizing KS statistic, the *KS test* is a nonparametric test of the equality of probability distributions that can be used to test whether a sample came from a given reference probability distribution, i.e., to test the goodness-of-fit.

Formally, for discrete data (as the cluster sizes in our case), the KS statistic is defined as the maximum distance between the cCDF of the empirical data and the cCDF of the fitted model:

$$D = \max_{\mathcal{S} > \mathcal{S}_{\min}} |F(\mathcal{S}) - F_{\text{model}}(\mathcal{S})| \quad (17)$$

Although commonly the KS statistic is defined between CDFs, it is equivalent to the above definition between cCDFs.

B. Fitting procedure

Provided that the lower bound \mathcal{S}_{\min} is known (the estimation of \mathcal{S}_{\min} is discussed later), the maximum likelihood estimator (MLE) of the power-law exponent τ is given by the solution to the transcendental equation:

$$\frac{\partial_{\hat{\tau}} \zeta(\hat{\tau}, \mathcal{S}_{\min})}{\zeta(\hat{\tau}, \mathcal{S}_{\min})} = -\frac{1}{n} \sum_{i=1}^n \ln \mathcal{S}_i \quad (18)$$

where $\{\mathcal{S}_i\}$ are all the observed cluster sizes $\geq \mathcal{S}_{\min}$. This is equivalent to maximizing the log likelihood function:

$$\mathcal{L} = -n \ln \zeta(\tau, \mathcal{S}_{\min}) - \tau \sum_{i=1}^n \ln \mathcal{S}_i \quad (19)$$

Though no closed-form solution exists for Eq. (18), one can reliably approximate τ as:

$$\hat{\tau} \simeq 1 + n \left[\sum_{i=1}^n \ln \frac{\mathcal{S}_i}{\mathcal{S}_{\min} - 1/2} \right]^{-1} \quad (20)$$

This approximation is substantially easier to compute and is accurate if \mathcal{S}_{\min} is not too small, with error decaying fast as $\mathcal{O}(\mathcal{S}_{\min}^{-2})$. If \mathcal{S}_{\min} is unknown, the estimation of \mathcal{S}_{\min} is the one minimizing the KS statistic:

$$\begin{aligned} \hat{\mathcal{S}}_{\min} &= \arg \min_{\mathcal{S}'} D(\mathcal{S}') \\ &= \arg \min_{\mathcal{S}'} \left(\max_{\mathcal{S}: \mathcal{S} > \mathcal{S}'} |F(\mathcal{S}) - F_{\text{model}}(\mathcal{S})| \right) \end{aligned} \quad (21)$$

C. Goodness-of-fit Test

To obtain the goodness-of-fit p -value, the commonly used procedure involves the following steps:

1. Take the KS distance between the empirical cCDF and the best fit, denoted as D_{real} .
2. Plug in the best-fit parameters $(\tau, \mathcal{S}_{\min})$ into Eq. (10) and generate a synthetic dataset of the same size as the original dataset. Calculate the KS distance between the synthetic cCDF and the best-fit model, denoted as D_{syn} .
3. The goal is to see if the obtained D_{syn} is comparable to D_{real} . For this, we repeat step (2.) M times ($M \gg 1$, typically $10^3 \sim 10^4$), each time generating a new synthetic dataset, eventually obtaining the $p(D_{\text{syn}})$ distribution. If D_{real} is close to the mode of $p(D_{\text{syn}})$ distribution, the power law is a considered plausible. M is set to 2500 to obtain all our reported p_{gf} .

4. Assign a p -value (p_{gf}) to the $p(D_{\text{syn}})$ distribution:

$$p_{\text{gf}} = \int_D^\infty p(D_{\text{syn}}) dD_{\text{syn}} \quad (22)$$

The closer p_{gf} is to 1, the more likely it is that the difference between the empirical data and the model can be attributed to statistical fluctuations alone. If p_{gf} is very small, the model is not a plausible fit to the data. Barabási [82] suggest the model is accepted if $p_{\text{gf}} > 0.01$, while Clauset *et al.* [80] suggest a harsher threshold of $p_{\text{gf}} > 0.1$. We adopt the latter.

Based on this calculation, we discuss goodness of fit results for different parameter values in the range $0.8 < \lambda < 0.9$. In Fig. 16, we plot the plausibility test values, p_{gf} , to identify parameter ranges where the power law is a good fit for the cluster size distribution data from simulations. The peaks of high p_{gf} values near λ_P and λ_A (filled circles in Fig. 16) show that the power law is a plausible fit only near the critical points.

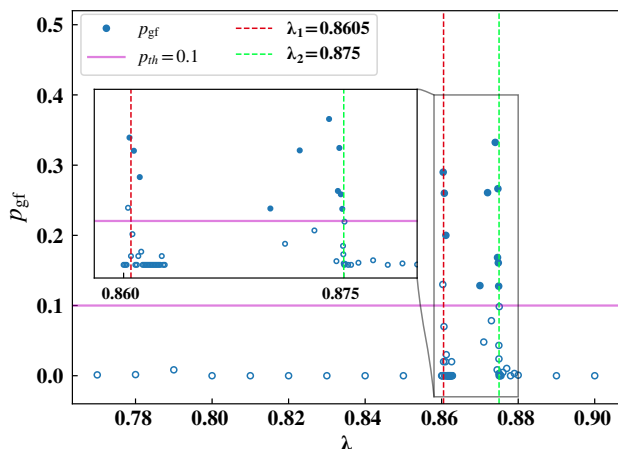


FIG. 16. **Power-law fits of cluster size distributions in the logistic GOL.** The (goodness-of-fit) p_{gf} values of the plausibility test for different λ values. In points with $p_{\text{gf}} > 0.1$, the hypothesis that the distribution follows a power law is favored. Note the clear peaks exceeding 0.1 close to λ_P and λ_A in the inset. The empty circles with $p_{\text{gf}} > 0.1$ denote points where the distribution passes the plausibility test, but *fails* the log-likelihood ratio test.

D. Model Comparison and Statistical Results

Even if we obtain a plausible power-law fit, it does not guarantee that the power law ($\propto x^{-\tau}$) is the best model. To rigorously assess its suitability, we must compare the power-law model against alternative fat-tailed distributions. Following the approach of Clauset *et al.* [80], we apply the KS method, including the following set of alternatives: power law with exponential cutoff, exponential, stretched exponential, and log-normal. The definition of these distributions is given in Table I.

Distribution Name	$f(x)$	C
Power law	$x^{-\tau}$	$(\tau - 1)x_{\min}^{\tau-1}$
Power law with cutoff	$x^{-\tau}e^{-\lambda x}$	$\frac{\lambda^{1-\tau}}{\Gamma(1-\tau, \lambda x_{\min})}$
Exponential	$e^{-\lambda x}$	$\lambda e^{\lambda x_{\min}}$
Stretched exponential	$x^{\beta-1}e^{-\lambda x^\beta}$	$\beta \lambda e^{\lambda x_{\min}^\beta}$
Log-normal	$\frac{1}{x} \exp\left[-\frac{(\ln x - \mu)^2}{2\sigma^2}\right]$	$\sqrt{\frac{2}{\pi\sigma^2}} \left[\text{erfc}\left(\frac{\ln x_{\min} - \mu}{\sqrt{2}\sigma}\right)\right]^{-1}$

TABLE I. Definition of the power-law distribution and other statistical distributions in our reference distribution set. For each distribution, we give the kernel $f(x)$ and the normalization factor C s.t. $\int_{x_{\min}}^\infty C f(x) dx = 1$.

A common method to compare models is the *likelihood ratio test* – to compute the likelihood of the data under two competing distributions, and take the logarithm of the ratio of the two likelihoods, denoted by \mathcal{LR} .

$$\mathcal{R} = \frac{\mathcal{L}_1}{\mathcal{L}_2} = \prod_{i=1}^n \frac{p_1(\mathcal{S}_i)}{p_2(\mathcal{S}_i)}$$

$$\mathcal{LR} = \ln \mathcal{R} = \ln \mathcal{L}_1 - \ln \mathcal{L}_2 \quad (23)$$

If \mathcal{LR} is positive, the first distribution is favored; if negative, the second distribution is favored; if close to zero, the data are insufficient to favor either model. We further apply the method proposed by Vuong [92] which gives a p -value (p_{LR}) that tells us whether the observed sign of \mathcal{LR} is statistically significant. If this p_{LR} -value is small (typically, $p_{LR} < 0.05$), then the sign is a reliable indicator of which model is a better fit to the data.

Table II presents the results of the *goodness-of-fit* and *log-likelihood ratio* tests, based on a sample size of $N = 5000$. Statistically significant p_{LR} -values are denoted in **bold**. Note that for *goodness-of-fit test results*, the larger the p_{gf} value, the more plausible the power-law model is. Whereas for *log-likelihood ratio test results*, the larger the p_{LR} -value, the less significant the sign of the test is. The final column lists our judgment of the statistical support for the power-law hypothesis at each critical point.

Alternatives to power law ($x^{-\tau}$) distribution	$\lambda_P = 0.86055$		$\lambda_A = 0.875$	
	LR	p_{LR}	LR	p_{LR}
Log-Normal ($\frac{1}{x} \exp \left[-\frac{(\ln x - \mu)^2}{2\sigma^2} \right]$)	-0.189	0.69	-0.41	0.54
Stretched exponential ($x^{\beta-1} e^{-\lambda x^\beta}$)	-0.97	0.61	-0.31	0.80
Exponential ($e^{-\lambda x}$)	373	0.001	27.6	0.005
Power law with cutoff ($x^{-\tau} e^{-\lambda x}$)	-3.89	0.005	-0.84	0.70
Verdict	Good support for power law with cutoff $p_{gf} = \mathbf{0.46}$		Good support for power law $p_{gf} = \mathbf{0.13}$	

TABLE II. The plausibility p_{gf} -values (*goodness-of-fit test*) for power-law and *log-likelihood ratio test results* between the power-law and alternative distributions at two critical points. Statistically significant p -values are denoted in **bold**. The plausibility values both exceeds 0.1, meaning the power-law is a plausible fit for both cases. LR is the log-likelihood ratio of power-law against alternative distributions: power-law with exponential cutoff ($\propto x^{-\tau} e^{-\lambda x}$), exponential ($\propto e^{-\lambda x}$), stretched exponential ($\propto x^{\beta-1} e^{-\lambda x^\beta}$), and log-normal ($\propto \frac{1}{x} \exp \left[-\frac{(\ln x - \mu)^2}{2\sigma^2} \right]$). If $LR > 0$, the power-law model is favored; if $LR < 0$, the alternative distribution is favored. The p_{LR} -value of log-likelihood ratio test denotes the significance of the *sign* of LR : if $p_{lr} < 0.05$, the *sign* of LR is considered significant. The ones at λ_P and λ_A indicates that power-law distribution is favored over exponential distribution. The other one at λ_P shows that power-law with exponential cutoff is favored over power-law. The final column lists the final judgments of the statistical support for the power-law hypothesis at each critical point: “with cutoff” means that the conclusion is power-law with exponential cutoff, while “good” indicates that the power-law is a good fit and none of the alternatives considered is favored.